Journal of Materials Research and Technology 43 (2026) 60–78

Contents lists available at ScienceDirect

Journal of Materials Research and Technology

journal homepage: www.elsevier.com/locate/jmrt

The effect of heat treatments on the elevated temperature mechanical performance of directed energy deposition repaired Ni-based superalloys

K.J. Samuel [a], N.C. Barnard [a], M. Jones [b], C.P. Heason [b], R.J. Lancaster [a,*]

[a] Institute of Structural Materials, Swansea University, Bay Campus, Swansea, SA1 8EN, United Kingdom
[b] Rolls-Royce Plc, PO Box 31, Derby, DE24 8BJ, United Kingdom

ARTICLE INFO

Keywords:
Alloy 718
Alloy 718Plus
Laser-blown powder directed energy deposition (LBP-DED)
Heat treatments
Mechanical properties

ABSTRACT

Laser-blown powder directed energy deposition (LBP-DED) is being explored for repairing forged Ni-based superalloy components. However, the high cooling rates associated with these processes develop an as-deposited microstructure that is distinct from that of the forged substrate. As such, elemental segregation, brittle interdendritic phases, and local mechanical mismatches can occur within these deposits. The current knowledge gap relates to how repair-compatible ageing heat treatments impact Alloy 718Plus deposits made on both forged Alloy 718 and forged Alloy 718Plus substrates, and if they can be utilised to enhance metallurgical compatibility while avoiding homogenisation heat treatments. For this reason, both forged substrates were repaired using Alloy 718Plus powder by LBP-DED and exposed to either Alloy 718 or Alloy 718Plus compatible ageing heat treatments. Microscopy, compositional analysis, electron backscatter diffraction, Vickers microhardness, tensile testing at 650 °C, and fractographic analyses were used to characterise the repairs. Both heat treatment conditions displayed distinct substrate, bond-line, heat affected, and LBP-DED repair zones. The repair deposit exhibited columnar dendritic grains with chain-like and granular interdendritic Laves phase remaining, indicating that the inherited as-deposited microstructure dominates the final microstructure. Heat treatment resulted in the precipitation of γ', as well as the local formation of η phase near Laves phase regions, yet did not significantly alter grain size or dendrite arm spacing. Additionally, the prior forged microstructure controlled epitaxial grain growth behaviours with larger forged Alloy 718 grains promoting larger LBP-DED grains. The 718-718Plus condition exhibited improved ductility at 650 °C compared to the 718Plus-718Plus condition. Fractographic analysis confirmed that failure occurred within the LBP-DED repair zone and was attributed primarily to strain incompatibility between the brittle Laves phase and the γ matrix. In summary, ageing heat treatment resulted in limited changes to the as-deposited Alloy 718Plus microstructure, whereas the substrate and as-deposited microstructures had more pronounced effects on the final metallurgical and mechanical behaviour.

1. Introduction

Nickel-based superalloys are a class of materials with excellent mechanical strength, high-temperature capability and stability, and corrosion resistance. These properties enable their use in arduous applications such as gas-turbine engines. Superalloys contain high concentrations of alloying elements including aluminium, titanium, chromium, tungsten, tantalum, molybdenum, and niobium [1]. One of the most widely used Ni-based superalloys is Alloy 718 (otherwise known as Inconel 718) and is largely used in gas turbine engine components in the forged condition at elevated temperatures. The microstructure of Alloy 718 conforming to AMS5662 [2] typically consists of a face-centred cubic (FCC) austenitic gamma (γ) matrix, which is strengthened by precipitates of gamma prime (γ') and gamma double prime (γ'') [3]. In addition to this, the microstructure includes delta phase (δ) and niobium and titanium carbides (MC), while Laves phase may form locally where segregation occurs during processing.

Rising turbine operating temperatures have intensified research into suitable materials. One response to this has been the development of Alloy 718Plus, a derivative of conventional Alloy 718 designed to address the latter's thermal stability limit of approximately 650 °C [4]. Alloy 718Plus offers enhanced thermal stability up to 704 °C, achieved

* Corresponding author.
E-mail address: r.j.lancaster@swansea.ac.uk (R.J. Lancaster).

https://doi.org/10.1016/j.jmrt.2026.06.061
Received 8 May 2026; Received in revised form 4 June 2026; Accepted 6 June 2026
Available online 8 June 2026

by promoting γ′ stability and reducing γ″ formation through additions of Al, Co, and W, together with modification of the Al/Ti ratio [5]. This enhancement makes Alloy 718Plus desirable for high-temperature gas-turbine applications. Although not yet widely implemented, Alloy 718Plus is considered a key next generation superalloy for future use [6]. Components of the gas turbine engine are prone to both wear and external damage due to foreign-object damage in service, leading to downtime and costly remanufacture. For this reason, repair of such forged components is of considerable importance.

Additive manufacturing (AM) has emerged as a transformative technology within the aerospace sector for improving the repairability of high-value components [7]. Unlike traditional subtractive methods, the AM process allows the creation of complex parts through layer-by-layer deposition of material, which minimises waste and production lead times. Among AM techniques, directed energy deposition (DED) has shown high compatibility for the repair of damaged critical components. Laser blown powder directed energy deposition (LBP-DED) typically employs a high-energy laser to create a molten pool in the substrate, into which metallic powder feedstock is deposited, enabling precise restoration of damaged parts [8]. However, the process itself in a repair context has yet to be perfected, since the layer-by-layer deposition introduces microstructural heterogeneity, particularly at the bond line zone between the deposit and forged substrate. Considering the repair of forged 718 and 718Plus, LBP-DED material solidification results in columnar grain structures with elemental segregation in the interdendritic regions, where elements such as Nb and Mo accumulate. This micro segregation leads to the formation of brittle phases, specifically Laves phase, which tend to degrade the mechanical performance of the LBP-DED repair zone and of the component as a whole [9–13]. This mismatch of properties between the forged substrate and LBP-DED repair material compromises the integrity of the repair. To mitigate these challenges, homogenisation heat treatments are often applied [14] to reduce chemical inhomogeneity and promote dissolution of detrimental segregated constituents such as Laves phase. However, with repaired components this is complicated since typical heat treatments would alter the forged material's microstructural and mechanical characteristics, limiting the heat treatments that can be applied. Moreover, since repairs are performed on machined components with strict dimensional tolerances, high-temperature and long-duration heat treatments may lead to unacceptable distortion. The ideal outcome is therefore to improve the homogeneity and performance of the LBP-DED material without significantly altering the forged substrate.

Homogenising the metallurgical and mechanical properties between the forged substrate and the deposited repair material would provide several advantages including reducing local differences in mechanical properties, improving load transfer across the bond line region, limiting strain incompatibility, and reducing stress concentrations during service. As a direct result of this homogenisation, improved tensile performance, fatigue life, and damage tolerance may be achieved in the repaired component. However, complete homogenisation typically requires high temperatures and long holding times to promote sufficient diffusion. These conditions may alter the forged substrate microstructure and mechanical properties by dissolving or coarsening beneficial precipitates, promoting over ageing or grain growth, and causing dimensional distortion of the repaired component, which is a crucial aspect to avoid. Therefore, in repair applications, the aim is not full homogenisation but a practical balance between improving the deposited material and preserving the original forged substrate condition.

To address these challenges, this study systematically investigates the microstructure and mechanical properties of forged Alloy 718 and 718Plus, repaired through LBP-DED exclusively with Alloy 718Plus. Specifically, the aims are to characterise the microstructural zones produced by LBP-DED repair, including the substrate, heat-affected, bond line, and deposited repair zone; determine how the Alloy 718 and standard Alloy 718Plus aging heat treatments affect phase formation, precipitate distribution, dendrite arm spacing and grain structure in the LBP-DED Alloy 718Plus material; evaluate how the initial forged substrate alloy and grain structure influence epitaxial growth and the resulting LBP-DED repair zone microstructure; compare the room-temperature and elevated-temperature tensile behaviour of the two repaired configurations; and to identify the dominant fracture mechanisms associated with Laves phase, precipitation state and deformation heterogeneity. By addressing these objectives, the study evaluates the suitability of Alloy 718Plus powder for repairing both forged Alloy 718 and forged Alloy 718Plus components using ageing-based post-process heat treatments.

2. Experimental

2.1. Material

The materials used in this study included forged Alloy 718 and forged Alloy 718Plus. Forged materials were obtained according to different standards: the Alloy 718 substrate conformed to AMS5662 [2], while the Alloy 718Plus substrate was manufactured to a proprietary standard. Alloy 718Plus powder was used for LBP-DED repair of both substrates. The 718Plus powder was produced via vacuum induction gas atomisation, had a powder size distribution of 53-106 μm, and was used in the virgin condition. The chemical compositions of the 718Plus powder used in this study (measured and nominal [15]), and the typical composition of Alloy 718 to AMS5662 standard, are presented in Tables 1 and 2. The nominal composition of forged Alloy 718Plus is proprietary and is therefore not shown below. The measured compositions were obtained from the average of multiple EDS measurements acquired from different regions of the sample, utilising a Hitachi SU3500 Scanning electron microscope.

2.2. Repair configurations and LBP-DED process settings

Two sample configurations were investigated.

1. Forged Alloy 718 substrate repaired with Alloy 718Plus using LBP-DED, denoted as 718-718Plus.
2. Forged Alloy 718Plus substrate repaired with Alloy 718Plus using LBP-DED, denoted as 718Plus-718Plus.

LBP-DED repair involved deposition of a 3 mm thick wall using optimised proprietary laser parameters. Rectangular blocks (55 mm × 26 mm) were fabricated for tensile analysis as depicted in Fig. 1 b). The chosen thickness ensured a representative LBP-DED zone volume and minimised excessive dilution from the substrate. Fig. 1 a) and c) shows how separate microstructural builds were created and sectioned for microstructural analysis, these were acquired from a block created with a different geometry. These microstructural blocks were made of forged material at the base (45 mm × 15 mm x 47.4 mm), towards the top it transitioned into a thin platform where the LBP-DED material was deposited with a deposition thickness comparable to the tensile blocks.

The process parameters for LBP-DED repair are summarised in equation (1) using Volumetric Energy Density (ED), to protect sensitive industrial values.

$$E_{vol} = \frac{P}{v \cdot h \cdot t} = 421.06\ \text{J} \Big/ \text{mm}^3 \quad (1)$$

2.3. Heat treatments

Post deposition, the rectilinear blocks were subjected to one of two heat treatment regimes. There are often limitations when conducting heat treatments on repaired materials as the effect on the substrate must also be considered. Generally, solution heat treatments are conducted on LBP-DED materials, however in a repair scenario this can result in distortion and/or altering of the forged substrate material properties,

Table 1
Measured and nominal elemental composition (wt.%) of 718Plus powder.

Element	Ni	Cr	Co	Mo	W	Nb	Al	Ti	Fe	C
Measured Alloy 718Plus	Bal.	17.9	9.1	2.7	1.0	5.5	1.5	0.74	9.5	0.03
Nominal Alloy 718Plus	Bal.	17-21	8-10	2.5-3.1	0.8-1.4	5.2-5.8	1.2-1.7	0.5-1	8-10	0.01-0.05

Table 2
Nominal elemental composition (wt.%) of alloy 718 (AMS5662).

Element	Ni	Cr	Co	Mo	W	Nb	Al	Ti	Fe	C
Alloy 718	50-55	17-21	1	2.8-3.3	-	4.8-5.5	0.2-0.8	0.65-1.15	18.5-20.0	0.08

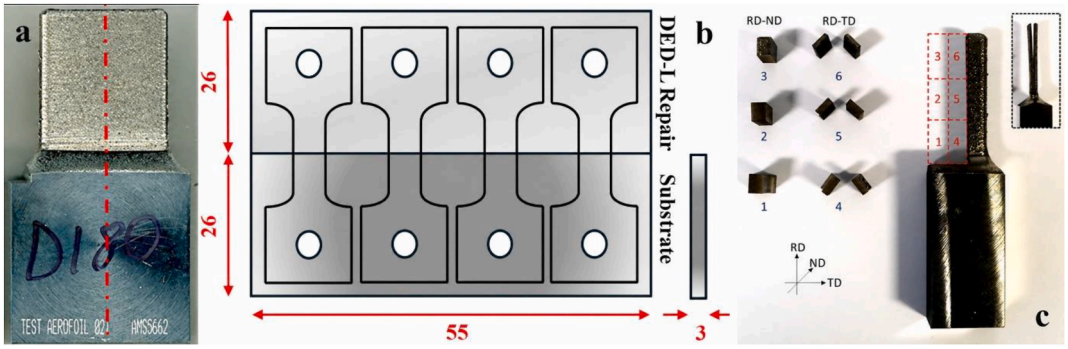

Fig. 1. A) Image and **b)** schematic representation of the LBP-DED rectilinear blocks and the layout of flat plate tensile specimens that were extracted (50 % LBP-DED repair, 50 % forged substrate), **c)** sectioning plan for microstructural analysis. All dimensions are in mm.

thus it is not always possible to carry out these types of heat treatments. Therefore, two ageing only heat treatments were selected for use in this experiment, chosen according to the substrate material and the differing needs thereof. The two repair configurations and associated heat treatments were not selected through a statistical design of experiments (DoE) approach but were instead selected based on application relevance and the heat-treatment requirements of the corresponding forged substrate materials. Referred to throughout as a 718 Standard (HTA) and 718Plus Standard (HTB), which is conducted at a higher temperature and longer durations than HTA. HTA is a proprietary heat treatment, whereas HTB was selected in line with the recommendations made by Kennedy [6] who explored the effects of similar heat treatments on the forged alloy. These selections were not intended to achieve full homogenisation between the substrate and deposit but were instead chosen as a repair compatible post-process heat treatment to improve precipitation strengthening in the repair zone. At the same time, they were chosen to limit changes to the forged substrate microstructure, reflecting the practical compromise needed in component repair.

Heating was conducted in a programmable box furnace under atmospheric conditions. The specimens were then machined to avoid surface oxides. HTA was applied to the 718-718Plus repaired specimens and HTB to the 718Plus-718Plus repaired specimens. The specimens are hereafter referred to as 718-718Plus HTA and 718Plus-718Plus HTB.

2.4. Microstructural analysis

Samples for microstructural analysis were prepared using a multi-stage grinding and polishing process to ensure surface smoothness and clarity. All samples were then etched using waterless Kalling's 2 reagent to reveal grain boundaries and secondary phases. To reveal the strengthening precipitates, a phosphoric electroetch was used. Phase fraction quantification was conducted using ImageJ software with the thresholding and image analysis features.

A Carl Zeiss Axial Observer inverted microscope was used to examine the general microstructure, porosity, and dendrite arm spacing (DAS) of the materials. For DAS measurement, approximately 50 measurements were taken for all sections of the materials, in both respective heat-treated states. For porosity, a minimum of 20 images encompassing a maximum of 50 % total surface area of each sample was explored.

A JEOL JSM 7800 F and a Hitachi SU3500 Scanning Electron Microscope (SEM) equipped with energy-dispersive X-ray spectroscopy (EDS) was employed to identify and characterise the phases present in the material, including γ', γ'', δ, η, metal carbides and Laves phase. EBSD scans were acquired under fixed operating conditions comprising aperture 1, a 20 mm working distance, 20 kV accelerating voltage, spot size 90, 1 μm step size, and 4 × 4 binning. The phase was assigned as "Ni Superalloy" during acquisition. Post-processing was carried out using HKL Tango Channel 5, where noise reduction was applied to reduce zero solutions. Grain reconstruction was conducted using a minimum grain size of 10 pixels, a critical misorientation angle greater than 10°, and a 2 % completion criterion. Grain boundary character was analysed separately using conventional definitions, with low-angle grain boundaries (LAGBs) defined as 2–15° and high-angle grain boundaries (HAGBs) defined as ≥15°. Sensitivity checks using a 15° reconstruction threshold did not change the comparative trends between conditions.

2.5. Mechanical testing

2.5.1. Microhardness Vickers testing

Microhardness Vickers testing was conducted using a Struers Duramin A40 microhardness machine with a 10-s dwell time and a load of 200 g. Measurements were taken from 2 mm below the bond line to 2 mm into the repair zone in 0.1 mm increments. This provided a minimum spacing of three indent diameters between adjacent indents, thus minimising interaction.

2.5.2. Tensile testing

Tensile tests were performed at both room temperature (20 °C) and elevated temperature (650 °C) in accordance with BS EN ISO 2002-1:2005 [16]. The tests utilised a 50 kN electric screw-driven machine

with the following parameters.

- Initial strain rate: 0.002 min^{-1}.
- Upon reaching 1.5 % strain, extensometry was removed and the remaining portion of the test was conducted under load conditions using a rate of 1.2 mm/min in order to preserve the extensometry equipment.

For elevated temperature tests, heat was applied using a digitally controlled furnace and was constantly monitored throughout the test by two Type N thermocouples with a tolerance of ±4 °C. Due to material availability constraints no repeat tests were performed, therefore, statistical scatter could not be calculated.

3. Results

3.1. Microstructural characteristics

Fig. 2 shows optical micrographs of the 718Plus-718Plus HTB and 718-718Plus HTA LBP-DED repairs after their respective heat treatments. In both specimens, three distinct microstructural regions can be identified: LBP-DED repair zone, the bond line zone/heat-affected zone (HAZ) and the substrate zone. The repair zone consists of columnar dendritic features that have grown epitaxially from the substrate in the build direction, together with a small amount of process-induced porosity. During LBP-DED, heat is dissipated into either the substrate or the previously deposited layers [17]. In addition, banded interlayer features are visible within the deposited region, consistent with repeated reheating and partial remelting during successive layer deposition [18]. At the bond line (Fig. 2aii)), the transition from the deposited material to the forged substrate is clearly visible. Directly beneath this interface, the substrate HAZ exhibits an equiaxed grain morphology, together with retained metallic carbides. Relative to the bulk substrate, the grains in the HAZ appear slightly enlarged, consistent with local thermal exposure during repair. This is examined further using EBSD in section 3.1.5. The same overall features are observed in the 718-718Plus HTA specimen, shown in Fig. 2b, including columnar dendrites, interlayer banding, a distinct bond line, and a substrate HAZ containing slightly coarsened grains and visible carbides. The principal difference between the two specimens lies in the forged substrate, with the 718-718Plus HTA sample exhibiting a much coarser equiaxed grain structure than the 718Plus-718Plus HTB sample.

3.1.1. Repair zone

SEM examination enabled more detailed characterisation of the repair zone microstructure. Fig. 3a shows the Laves phase (Ni, Fe, $Cr)_2$(Nb, Mo, Ti) distribution within the repair region of the 718-718Plus HTA specimen. As both repair configurations used the same deposited alloy (718Plus) and identical deposition parameters, the morphology and distribution of the Laves phase were broadly similar in both specimens. The phase was predominantly observed as an interconnected, chain-like constituent located in the interdendritic regions, although locally more granular morphologies were also present. Even where the morphology was more discrete, the particles generally remained aligned with the dendritic solidification structure. The Laves phase is a brittle intermetallic phase that forms via the eutectic reaction L → γ + Laves phase [19–21], in the final stages of solidification. The phase is also expected to remain stable under the applied heat treatments, given its high solvus temperature of approximately 1150 °C [22]. The Laves phase formed in the interdendritic regions of the repair zone and is made up of high amounts of Nb, forming once the wt.% exceeds 10-12 % [23]. There are however several factors which contribute to the Laves phase characteristics present in this material. Firstly, 718Plus tends to have a relatively high amount of Nb. Secondly, due to the nature of the LBP-DED process and the rapid heating and cooling of several layers that ensues, the local materials undergo non-equilibrium solidification. Within this process, Nb tends to segregate to the interdendritic regions due to its limited solubility in the γ matrix. This behaviour may be described using the segregation coefficient (K) which is a measure of how a specific element distributes between the solid and liquid phases during the solidification process, as shown in equation (2):

$$K = \frac{C_s}{C_l} \tag{2}$$

Where C_s is the concentration of the element in the solid phase and C_l is the concentration of the element in the liquid phase. Elements with $K <$

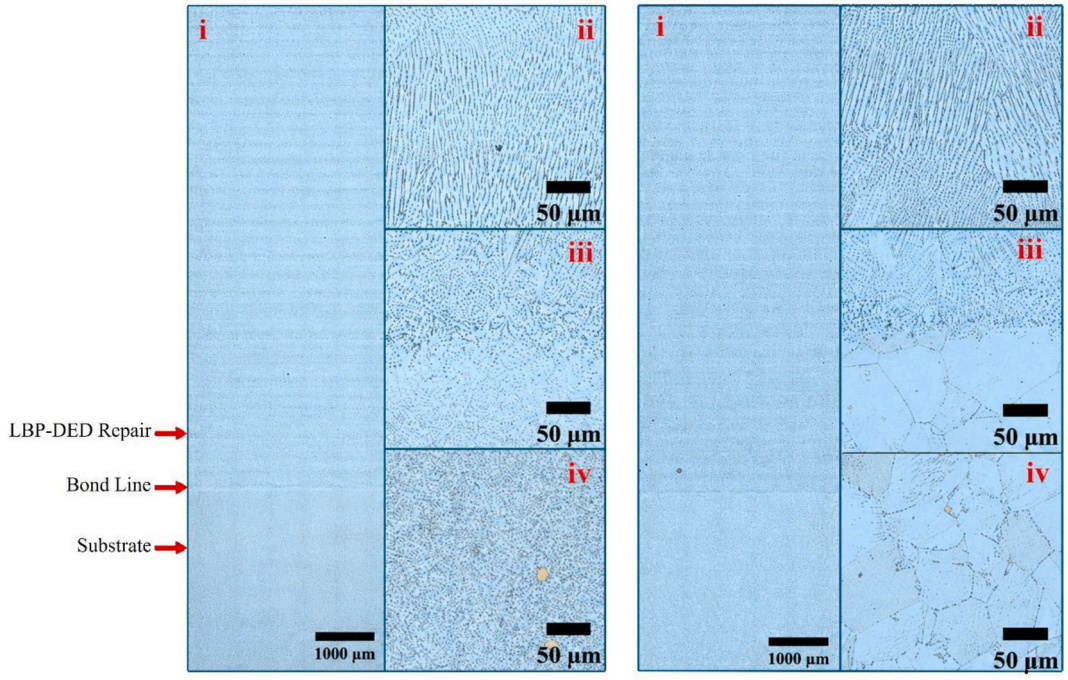

Fig. 2. Repair Microstructure of **a)** 718Plus-718Plus HTB and **b)** 718-718Plus HTA. **i)** overview, **ii)** repair zone, **iii)** bond line zone, and **iv)** substrate zones.

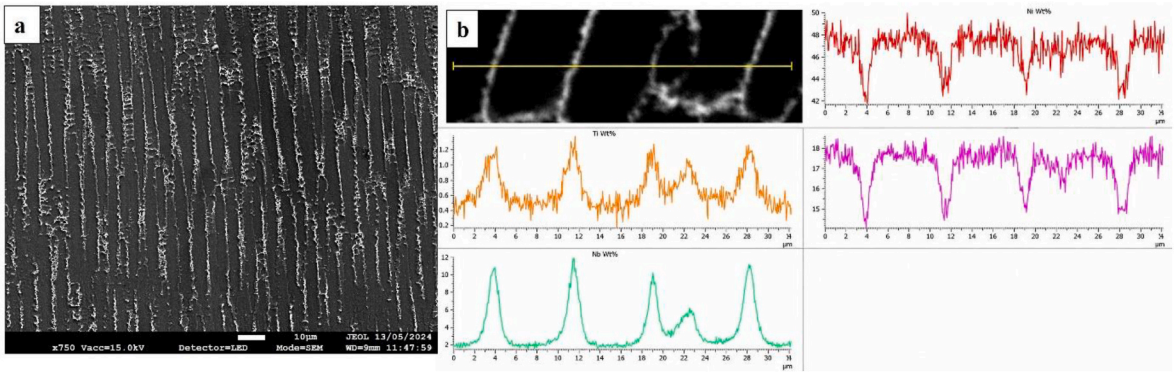

Fig. 3. A) Laves phase morphology and distribution in 718Plus HTB LBP-DED material and b) EDS analysis wt.% line scans showing elemental micro segregation in the interdendritic regions of 718Plus HTB repaired material.

1 are rejected to the remaining liquid and therefore concentrate in interdendritic regions, while $K > 1$ means the element preferentially enters the solid dendrite. In this alloy, the refractory elements such as Nb, Mo and to some extent Ti, have partition coefficients below unity, and thus are rejected to the interdendritic liquid during solidification. This local enrichment drives formation of Nb/Mo-rich intermetallics such as the Laves phase during the final stages of solidification. By contrast, base elements such as Ni, Cr and Fe partition preferentially into the primary γ dendrites. The overall effect in LBP-DED builds often results in strong interdendritic segregation and Laves phase formation [24] once the critical concentration needed is achieved, solidifying as a eutectic-like structure (γ/Laves) at around 1150 °C.

EDS analysis confirmed interdendritic enrichment and the presence of Laves phase, with area fraction values shown in Table 3. Fig. 3b shows the elemental micro segregation of Ti and Nb to the interdendritic regions as well as the corresponding drops in Cr and Ni in the same region when compared to the γ dendrite matrix. EDS point scans showing the elemental spectra of both the Laves phase and γ matrix are shown in Fig. 4 b) and c) respectively, again showing elevated wt.% concentrations of Nb with decreased Ni, Cr and Fe in comparison to the γ matrix, further confirming identification of this phase as Laves. This trend was consistent between the specimens in the repair zone due to the same repair material being used with identical processing parameters.

The ageing treatments in both repair configurations produced γ′ and γ″ (although primarily γ′) precipitates, as shown in Fig. 5a). However, the precipitation was non-uniform, with γ′ and γ″ preferentially precipitating near the interdendritic regions and the Laves phase. This is consistent with the segregation of elements to this region, specifically Ti and Nb. γ′ is an ordered $L1_2$ (cubic) crystal structure precipitate of Ni_3(Ti, Al). Therefore, Ti being segregated to these interdendritic regions in the as-built condition results in their precipitation here when aged. Furthermore, although Ti and Al are the main contributors to the formation of the γ′ precipitates, it has been shown that Nb can partially substitute for Ti in this phase [25], which further mechanically strengthens the phase due to a mismatch of atomic size and greater atomic weight, thus hindering dislocation motion to a greater degree. Fig. 5b) illustrates this non-uniform precipitation effect around the Laves phase, with decreasing precipitates near the core of the dendrites.

Additional minor phases were also present in the repair zone of the 718Plus material in both HT conditions, specifically eta (η) (Ni_6(Al, Ti) Nb) phase. η was found to precipitate in the interdendritic and Laves phase regions. Considering the chemical formula, it can be deduced that this is due to the need for elements such as Ti and Nb, both of which have segregated to this interdendritic region, while being depleted of it in the dendrite core due to the previously mentioned processing conditions and material characteristics. Asala et al. [26] reported a similar compositional preference for η phase precipitation, specifically Nb, which would explain the location preference for η growth shown in these results. The η phase exhibits a needle-like morphology and appears to grow from the Laves phase itself, forming a Widmanstätten-like structure, as seen in Fig. 6. The Laves phase may act as a nucleation site for the η phase during ageing. Nb secured in the Laves phase is likely diffusing and recombining with Ti thereby forming η phase. This is often referred to as transformation-induced precipitation [27] and explains why with ageing, η grows, which relates to a key difference between the two repaired materials, namely ageing temperature and duration. The HTA repair material (718-718Plus HTA) had a lower amount of η phase present in the repair zone compared to the HTB specimen (718Plus-718Plus HTB), however, accurate quantitative measurements of this were difficult due to Laves phase vicinity interfering with calculations and the extreme small scale required did not allow for accurate quantification. Nevertheless, only a few instances of η phase were observed in the HTA repair zone compared to several in the HTB material. The higher temperatures and longer durations of the HTB heat treatment may allow more diffusion of Nb from the Laves phase and therefore an increased transformation into η phase. γ′ precipitate size was similarly influenced by the ageing conditions, with a finer precipitate size in the HTA specimen and coarser precipitates in the HTB material.

Table 3
Area volume fraction (%) of Laves phase in Repair Zone and eta/delta phase in respective substrate zones.

Heat Treatment	Laves Phase (%) Repair Zone	Eta/Delta (%) Substrate Zone
718Plus-718Plus HTB	3.36	4.16
718-718Plus HTA	2.81	0.13
718Plus-718Plus As-Built	2.28	3.73
718-718Plus As-Built	2.03	0.26

3.1.2. Substrate

The microstructure of the substrate zones varied between 718 and 718Plus HTA and 718Plus-718Plus HTB LBP-DED repaired samples, due to the different forged substrate alloys used. Considering first the phases present in the 718Plus forged substrate, blocky Nb and Ti carbides were dispersed throughout the substrate zone. EDS analysis confirmed elevated concentrations of Nb and Ti in these carbides, as shown in Fig. 7, where the MC-type carbides differ in morphology. The NbC blocky carbides appear as bright features, whilst the TiC carbides appear darker and more rounded. Other phases present include γ′ and γ″, which appear uniformly dispersed in the substrate, which is expected due to the optimised processing and heat treatment conditions of the forged material.

Additionally, η phase is precipitated at the grain boundaries in a more rod-like morphology distinctly different from the repair zone. The

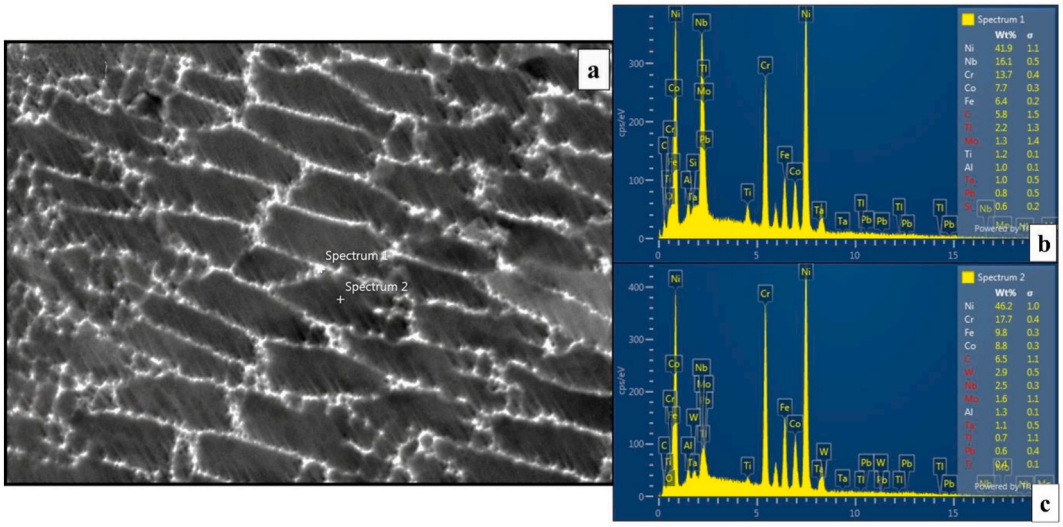

Fig. 4. Point scans of 718Plus-718Plus HTB repaired specimen **a)** overview **b)** Laves phase spectrum **c)** γ matrix spectrum.

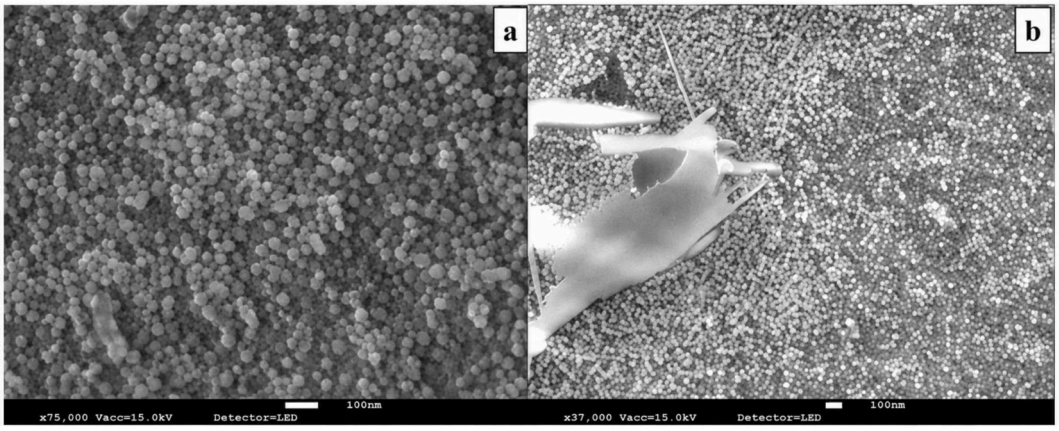

Fig. 5. 718Plus-718Plus HTB repaired specimen **a)** γ′ precipitation in the 718Plus LBP-DED repair zone, **b)** non-uniform precipitation around the Laves phase.

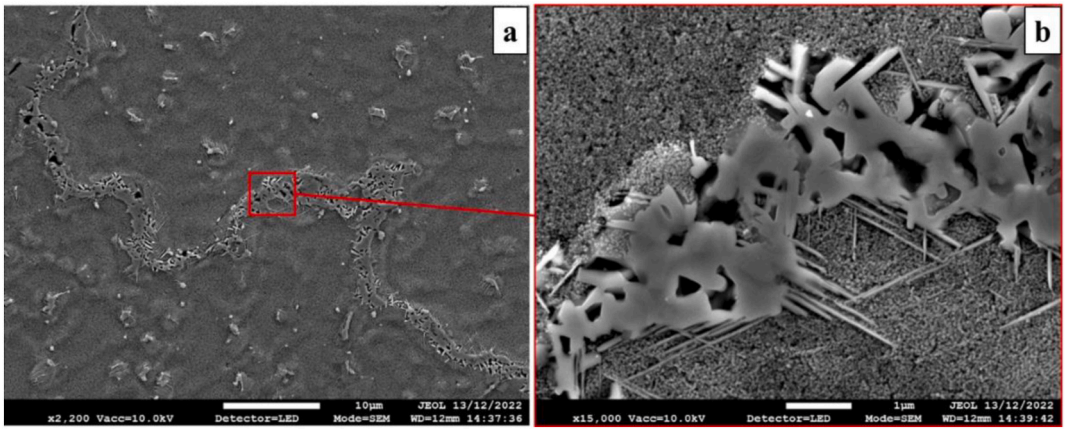

Fig. 6. Widmanstätten-like constituent in 718Plus HTB LBP-DED repair zone.

precipitation at the grain boundaries is related to the typical precipitation mechanism of the η phase itself, since there is discontinuous precipitation nucleated at vacancies and stacking faults as well as other defects in the material, often in conjunction with the transformation of the γ′ precipitates or depletion of the supersaturated γ-matrix. As discussed by Li et al. [28] the grain boundary preference is a result of higher vacancy density at grain boundaries in the material as well as some segregation of the forming elements of the phase (namely Ti and Nb to the boundaries), thus the phase both nucleates and grows during the previous heat treatment and ageing process of the forged material. The difference in morphology of the η phase in the repair zone and the substrate zone can be related to the Blackburn relationship as discussed

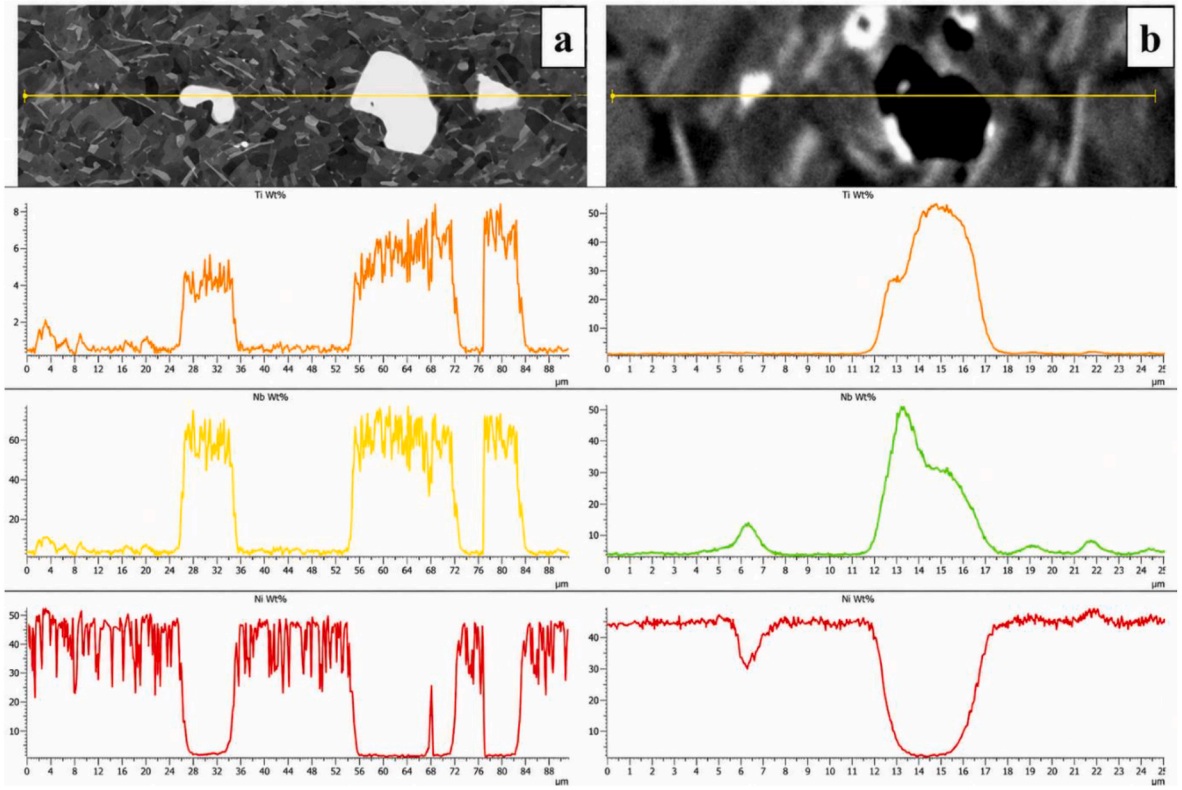

Fig. 7. Carbides in the 718Plus forged substrate (from 718Plus-718Plus HTB sample), **a)** NbC and **b)** TiC.

previously [29–31]. The Blackburn relationship is a specific orientation behaviour between the η phase and the γ matrix, where the η phase has a semi-coherent interface with the γ matrix with growth being preferred longitudinally due to the hindered migration of elements along the width of the phase and a lack of available forming elements surrounding it due to the inhomogeneous distribution of Ti and Nb in the repair zone. Whereas the homogenous distribution in the substrate zone allows for easier elemental diffusion to the η phase, thus allowing thickening of the width of the phase, which subsequently results in the thicker plate shaped morphology observed in this study.

The 718 forged substrate (found in the 718-718Plus HTA sample) showed similarities to the forged 718Plus substrate in terms of the carbides present. Both Nb carbides and Ti carbides were found, as shown in Fig. 8. The carbides exhibited high concentrations of Nb and Ti respectively, as well as the typical lighter and darker appearance in SEM imaging. In addition to this, there is no evidence of η phase being present; however, a needle-like grain boundary phase consistent with orthorhombic δ (Ni_3Nb) was observed, in accordance with the expected precipitation behaviour of Alloy 718. δ phase and γ″ are typically favoured in 718 rather than η phase and γ′, due to the differences in chemical composition. Higher Nb, lower Ti and Al content which are the forming elements of γ″ and both η phase and γ′ respectively, makes formation of the γ″ and δ phase favourable and the formation of γ′ and η unfavourable. δ phase tends to precipitate within a temperature range of 650 °C to 980 °C, which aligns with the typical ageing temperature of forged 718 to the AMS5662 standard [2]. During forging, recrystallisation and deformation processes will enhance the δ phase precipitation, with cooling from forging temperatures allowing Nb segregation to grain boundaries promoting grain boundary δ phase formation.

3.1.3. *Bond line and HAZ zone*

The bond line and HAZ zone of the 718Plus-718Plus HTB LBP-DED repaired specimen is shown in Fig. 9. As shown, there is limited evidence of η phase in the HAZ zone directly under the bond line, followed

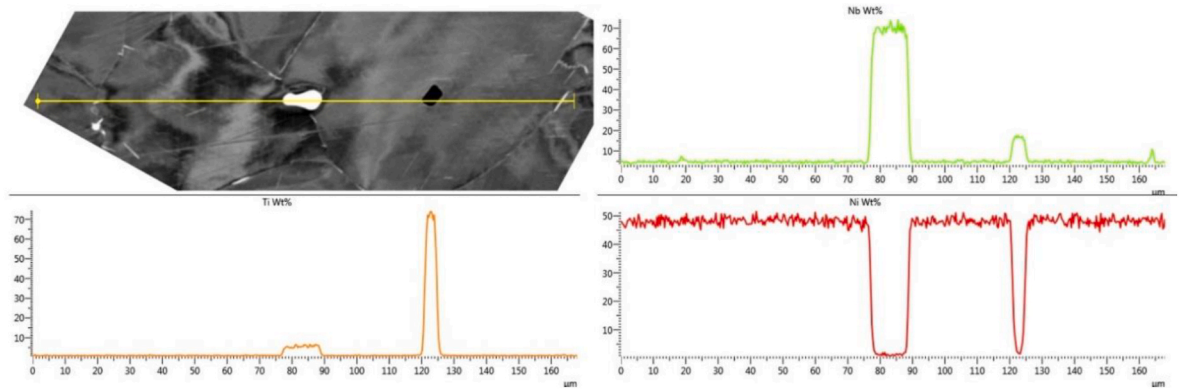

Fig. 8. EDS line scan of carbides found in the 718 forged substrate of 718-718Plus HTA.

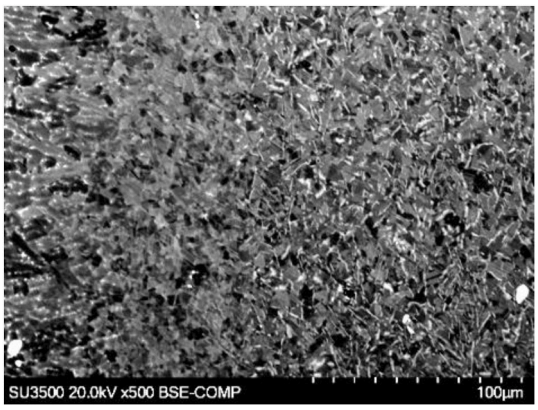

Fig. 9. Bond Line and HAZ Zone of 718Plus-718Plus HTB LBP-DED repaired specimen.

by the resumption of the phase with an increasing distance into the substrate forged material. However, carbides remain visible in the HAZ as shown by the lighter and darker blocky particles, with similar morphology to those of Fig. 7. The reduced η phase content is likely due to the elevated temperatures achieved during LBP-DED. During deposition of the first layer, the local thermal cycle may exceed the η phase solvus temperature (~980-1000 °C) [32], allowing for partial dissolution, with rapid heating and cooling by successive layers being insufficient to reform the phase. The following HTB treatment likely precipitates the phase slightly, however, as evidenced by the imaging, this appears to be limited. Additionally, the repair process may locally modify composition and grain structure within the HAZ. The diffusion of η phase forming elements in the HAZ makes the nucleation and growth during subsequent ageing less favourable. As discussed, there are carbides still present within the HAZ but less frequently than in the bulk of the substrate. Again, this is likely due to the elevated temperatures achieved in the LBP-DED repair process, which may be high enough to induce constitutional liquation of the NbC carbides in this region of the substrate. This, in conjunction with the Nb segregation that will occur due to the rapid heating and cooling of the process, leads to what appears to be a Nb-rich liquid film on the HAZ grain boundaries, with a composition similar to that of the Laves phase, essentially 'locking' some of the available Nb in place leading to a lack of η phase precipitation in subsequent ageing heat treatment.

The 718-718Plus HTA LBP-DED repaired specimen exhibited a more distinct bond line with a clear differentiation between the substrate and the repaired zones as shown in Fig. 10a. Once again, a lack of grain boundary precipitates, in this case δ, is seen in the HAZ but with some carbides remaining. A similar effect is likely occurring with dissolution of the δ phase due to the elevated temperature processing inherent to LBP-DED. Nb-rich grain boundaries are again seen in the HAZ as shown

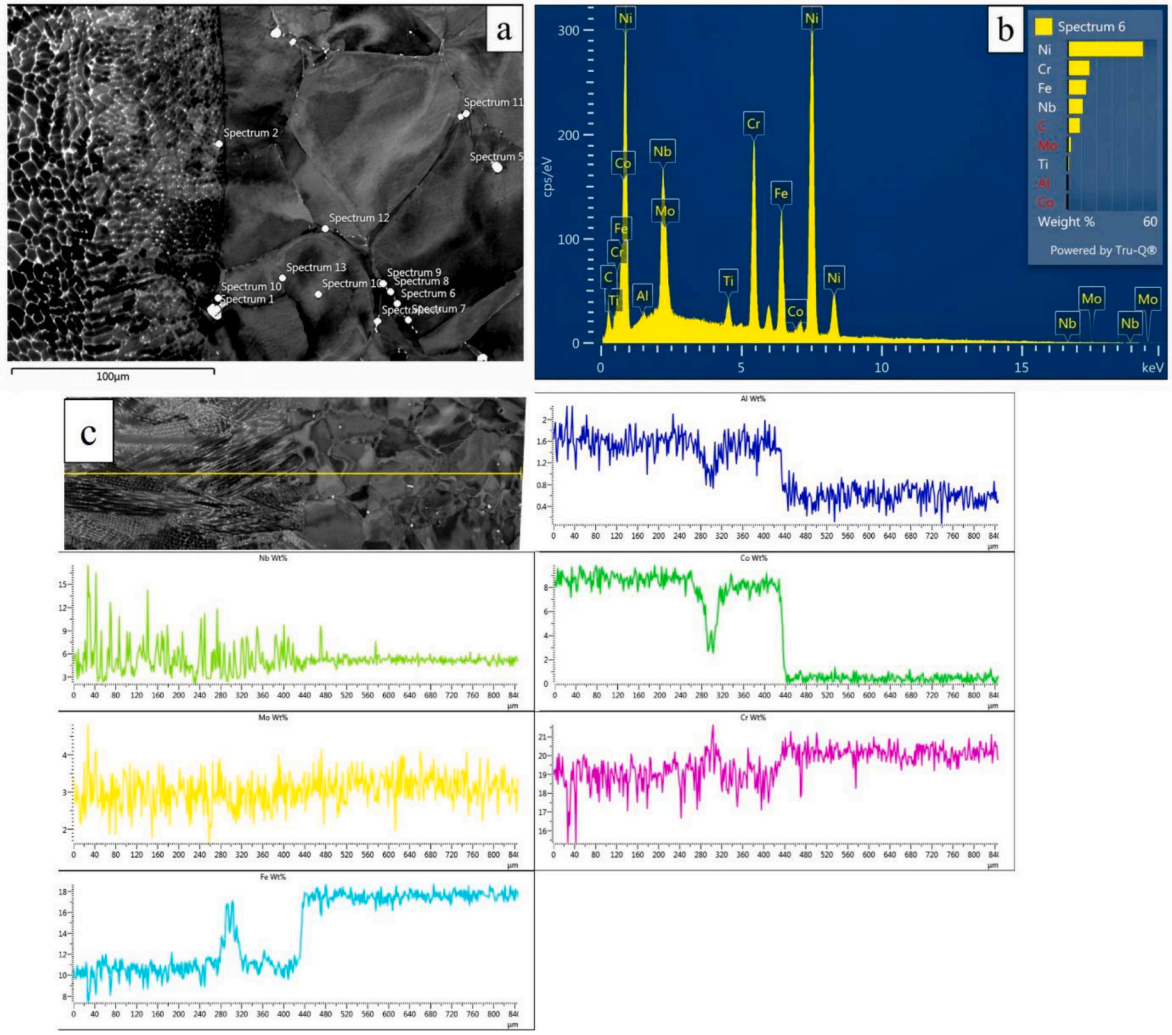

Fig. 10. A) Bond line and HAZ of 718-718Plus HTA LBP-DED repaired specimen showing Nb-rich grain boundary carbides. B) Associated spectra of Nb-rich grain boundary and c) EDS line scan of 718-718Plus HTA specimen across the bond line region.

in the EDS spectra in Fig. 10 b). This is also consistent with Nb segregation to the grain boundaries due to the high temperatures inducing Nb segregation and constitutional liquation of some of the carbides in this zone.

One notable difference between the two repaired specimens is when examining the composition of the bond line on a larger spatial scale. A compositional difference is observed when transitioning from the 718 substrate to the 718Plus repaired material, whereas this behaviour is not seen in the 718Plus-718Plus HTB repaired specimen, where the element composition remains relatively consistent. Fig. 10c shows this composition change in the 718-718Plus HTA repaired specimen, and shows that the Nb content starts to decrease in the HAZ and with increasing depth into the substrate material. This can be explained via the standard dispersion of the element in the forged material creating the consistent level in the substrate. The spikes in the HAZ are attributed to the previously discussed effect of the laser segregating Nb in the HAZ and creating Nb-rich grain boundaries. Finally, the very high peaks in the repair zone can be explained by the strong Nb segregation and Laves phase formation in the material. The decrease in Al and Co as the line moves into the substrate is simply due to the decreased content of these elements in the 718 substrate, with the increase in Fe explained by its respective increased content in the 718 substrate. As mentioned, the 718Plus-718Plus HTB repaired specimen showed a more consistent elemental composition between forged substrate and repaired material (predominantly owing to the fact that they are the same material), however, it displayed similar characteristics in Nb composition, with a more consistent level in the substrate, some spikes in the HAZ and larger fluctuations in the LBP-DED material due to the Laves phase.

3.1.4. Dendrite arm spacing (DAS)

The measurement of DAS of both 718Plus HTA and 718Plus HTB repair specimens was systematically analysed in their respective heat-treated states to determine whether any variation was present due to the differing heat treatment times and temperatures applied. The method adopted is displayed in Fig. 11, with a minimum of 50 measurements taken from comparable sections on the XZ face of the specimens. Different build heights were also examined to assess if DAS evolved with increasing build height. The HTB specimen exhibited a slightly larger DAS in comparison to the HTA specimen at both a lower and higher build height. Furthermore, the HTB specimen showed a slight increase in average DAS with increasing build height (approximately 0.5 μm increase), whereas the HTA specimen decreased slightly at lower build heights (approximately 0.2 μm decrease). The differences in DAS at different build heights can possibly be attributed to the thermal gradients, through the localised reheating and solidification dynamics of the LBP-DED process. At higher build heights there is more reheating and less impact of the substrate which acts as a heat sink. Therefore, an increase in DAS with build height would be expected, as also reported by Zhai et al. [33], although this would require further verification here through a comprehensive build assessment. Therefore, the differences seen between the HTB and the HTA specimens are most likely attributable to inherent variability in the AM process, rather than the applied heat treatment.

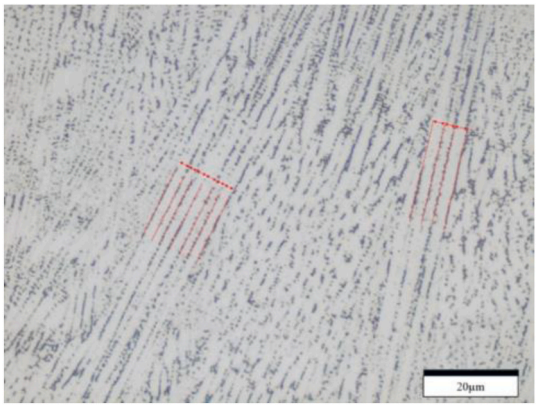

Fig. 11. Illustration of DAS measurement.

3.1.5. Grain analysis

EBSD maps of the different samples are presented in Fig. 12. Each map shows three distinct zones, labelled the substrate for the forged material, the transition zone which represents the LBP-DED material in the immediate vicinity of the forged material i.e. slightly above the bond line, and finally the LBP-DED zone which represents the bulk of the additive repair material. The difference between these zones is pronounced, since the substrate has the grain structure of the forged material showing equiaxed grains with weak texture. The bond line transition zone shows the start of epitaxial columnar grain growth, increasing in size with increased depth into the bulk LBP-DED zone, but with weaker texture than the bulk LBP-DED zone. This is consistent with epitaxial growth and reduced heat input (due to the heat sink effect) causing some orientation memory of the equiaxed grains it is deposited on. Finally, the LBP-DED zone shows larger columnar grains with a visibly stronger texture, resulting from high thermal gradients and low solidification rates along the build axis, with the texture a result of preferential grain growth in accordance with low interfacial energy, in addition to the repeated thermal cycling of the LBP-DED process. Grains orientated away from the induced thermal gradient of the LBP-DED laser grow slowly or become hindered, whereas grains aligned to the heat flow direction grow faster and outcompete neighbouring grains, continuing layer after layer further reinforcing texture with increased build height [34] [18].

To explore this quantitatively, grain properties were analysed for each of the zones in both specimens using the EBSD maps. The results are shown in Table 4, which also includes further measurements recorded in the forged substrate material. The 718Plus-718Plus HTB LBP-DED repaired specimen shows a clear trend in increasing grain area and diameter starting with the smallest in the substrate, followed by a slight increase in the HAZ zone (which is within the substrate directly below the bond line) consistent with heat input of the laser causing grain growth, followed by increased values in the transition zone (which is within the LBP-DED material just above the bond line) and the highest area and diameter achieved in the LBP-DED zone. Aspect ratio is also an important parameter; in Channel 5 software aspect ratio is defined as the ratio of the major axis to the minor axis, such that a value of 1 represents a perfectly circular grain and larger values indicate increasingly elongated morphologies. In the present study, these values were inverted to yield a scale between 0 and 1, such that lower values indicate greater grain elongation. Accordingly, the LBP-DED zone exhibits the lowest aspect ratio, consistent with its elongated columnar grain structure, whereas the transition zone above the bond line exhibits a slightly higher aspect ratio, and the substrate and HAZ in the substrate exhibit the highest aspect ratios, reflecting the more equiaxed grain morphologies observed in these regions.

The 718-718Plus HTA LBP-DED specimen shows a slightly different trend. The grain size in the substrate was shown to be significantly larger than that of the additive grains (and also significantly larger than those present in the 718Plus-718Plus forged material), and therefore, a statistically representative number of grains could not be analysed from the EBSD images shown in Fig. 12. Thus, only the substrate grains from a separate EBSD with significantly lower magnification were used, resulting in a lack of HAZ grains in Table 4 for this specimen. However, examining the transition zone above the bond line and LBP-DED zone of the specimen, a similar trend to the 718Plus-718Plus sample is observed. Lower grain area and diameter size is seen in the transition zone above the bond line attributable to the heat sink effect, with larger grains seen in the bulk LBP-DED zone. Regarding aspect ratio, the transition zone above the bond line and LBP-DED zone in this specimen were

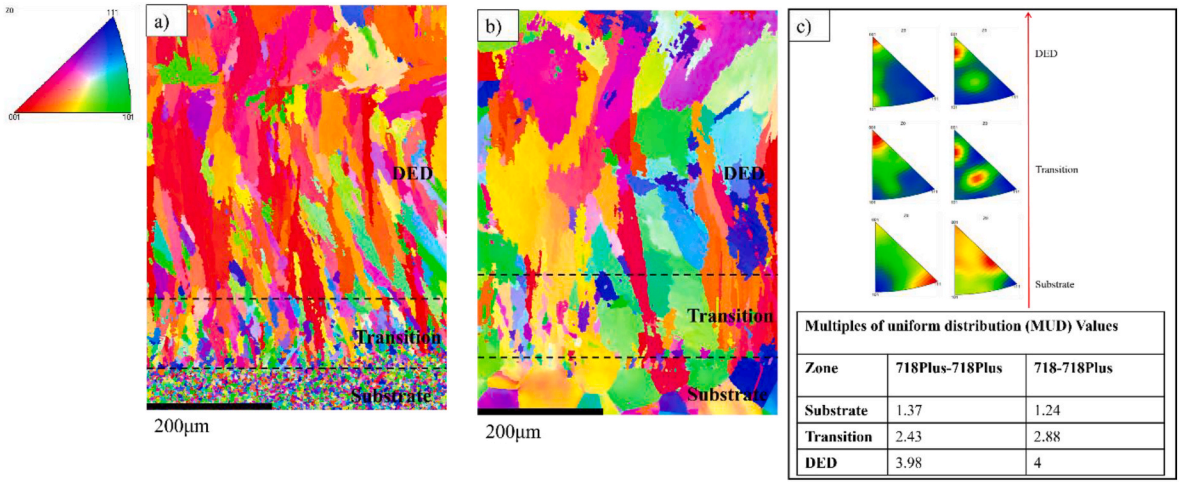

Fig. 12. EBSD inverse pole figure maps of **a)** 718Plus-718Plus HTB LBP-DED and **b)** 718-718Plus HTA **c)** inverse pole figures of the different materials and respective MUD values.

Table 4
Average grain size measurements of each region of the LBP-DED 718Plus-718Plus and 718-718Plus specimens, both in the as-built and HT condition (either HTA or HTB).

Zone	718Plus-718Plus HTB LBP-DED				718-718Plus HTA LBP-DED			
	Area (μm^2)	d (μm)	Aspect ratio	LAGB (%)	Area (μm^2)	d (μm)	Aspect ratio	LAGB (%)
Substrate	13.75	3.72	0.51	3.07	2188.6	41.12	0.50	2.94
HAZ	16.79	4.07	0.62					
Transition	72.32	6.96	0.46	10.83	341.63	11.18	0.45	18.89
DED	233.74	10.08	0.38		402.42	12.04	0.48	
Zone	**718Plus-718Plus As-Built LBP-DED**				**718–718Plus As-Built LBP-DED**			
	Area (μm^2)	d (μm)	Aspect ratio	LAGB (%)	Area (μm^2)	d (μm)	Aspect ratio	LAGB (%)
Substrate	10.03	3.79	0.5	2.78	2147	42.73	0.47	2.81
HAZ	10.19	3.17	0.52					
Transition	109.05	8.23	0.44	10.25	277.23	9.3369	0.44	18.46
DED	341.75	12.80	0.43		340.71	11.035	0.41	

comparable, with the bulk LBP-DED grains showing a slightly decreased aspect ratio. Comparing the two alternative substrate materials (HTB 718Plus and HTA 718) the average grain sizes are significantly different, with the forged 718 HTA exhibiting a much larger grain size, more than a 2174 μm^2 difference. This is observed, but to a lesser degree, throughout the LBP-DED repaired microstructure, with the 718-718Plus specimen showing a larger grain size in comparison.

To further explore the developed texture in the specimens, inverse pole figures (IPF) were recorded from the EBSD data considering mainly the transition and LBP-DED zones, as this is where texture is predominantly observed. These were used to calculate multiples of a uniform distribution (MUD) value. The IPF maps and corresponding MUD values for each heat-treated specimen are shown in Fig. 12c). As discussed earlier, neither heat treatment has led to any recrystallisation, and the microstructures are relatively consistent with their as-built state. This was proven by comparing the as-built EBSD maps to the respective heat-treated EBSD maps, which showed similar values for grain area, diameter, aspect ratio and texture, as shown in Table 4. Therefore, the observed texture appears to be attributable primarily to the LBP-DED process. A common relationship is seen in both heat-treated samples, where the substrate zone shows low texture, with MUD values below 2, whereas with increasing distance through the transition zone and the bulk LBP-DED zone, the MUD values steadily increase, peaking in the bulk LBP-DED grains, but remaining below 4. Although no ASTM or ISO standard currently exists for MUD values and texture correlation, the results indicate an increase in <001> orientated texture from the substrate, transition and into the LBP-DED zone, as would be expected in primarily FCC material with the thermal history that exists due to the LBP-DED process.

3.2. Porosity

Via optical microscopy, porosity analysis revealed notable differences in pore distribution in the different regions of the samples. A higher density of porosity was observed in the LBP-DED repair material in the vicinity of the bond line in both HTB and HTA specimens, as shown in Fig. 13, with no significant difference in porosity between the two heat treatments. In both instances, the high density of porosity observed near the bond line gradually decreased with increasing build height, suggesting improved deposition quality as build height increases. However, this high density of porosity creates cause for concern as a localised concentration of defects may act as an area of stress raisers when subjected to mechanical loading, therefore adversely affecting the properties. Most of the porosity was gas porosity evident by its circular morphology, with some lack of fusion (LoF) features present but to a much lesser extent.

3.3. Mechanical properties

3.3.1. Microhardness Vickers

Fig. 14 shows the microhardness Vickers variation from the substrate, through the HAZ and bond line and into the LBP-DED repaired zone for both 718-718Plus HTA and 718Plus-718Plus HTB specimens, after their respective heat treatments have been applied. Each indent

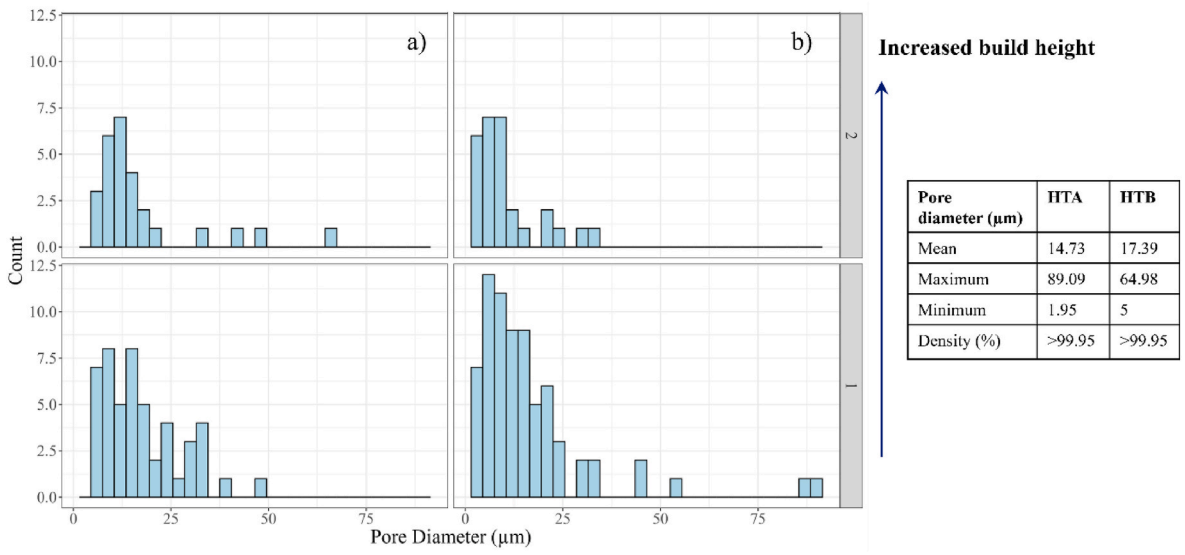

Pore diameter (μm)	HTA	HTB
Mean	14.73	17.39
Maximum	89.09	64.98
Minimum	1.95	5
Density (%)	>99.95	>99.95

Fig. 13. Pore size distribution with build height **a)** 718Plus-718Plus HTB **b)** 718-718Plus HTA.

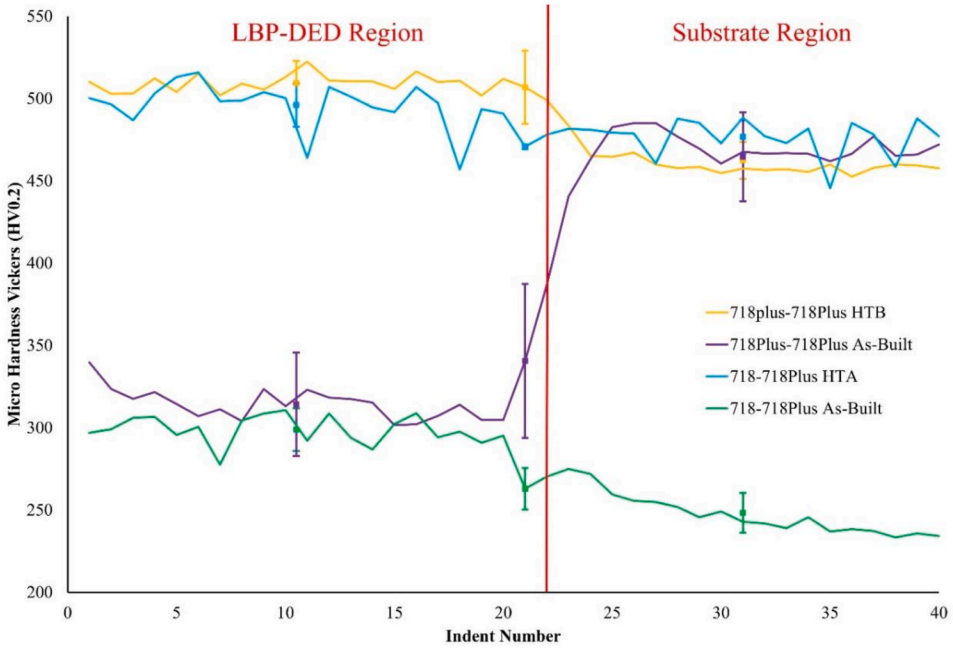

Fig. 14. Microhardness Vickers variation with location in repaired. Each respective indent is 0.1 mm apart.

was spaced 0.1 mm apart to produce a localised characterisation of the different regions. For both specimens, a slight increase in microhardness Vickers was observed in the LBP-DED region, with the HTB specimen showing a slightly higher average microhardness Vickers in this zone which is consistent with the longer ageing times and higher temperatures promoting further precipitate development, albeit despite exhibiting a larger grain size. However, the forged substrate material showed a different behaviour with the 718 material (HTA) showing slightly higher microhardness Vickers than the 718Plus forged material (HTB) after the heat treatments. The higher microhardness Vickers of the 718 substrate is consistent with differences in precipitation behaviour between Alloy 718 and Alloy 718Plus. 718 has favourable conditions to primarily precipitate γ'' which leads to a higher mechanical strengthening effect at room temperature for an array of reasons. γ'' has a body-centred tetragonal (BCT) structure, aligned along dislocation lines which leads to significant coherency strain fields in the γ matrix creating mechanical strengthening through lattice distortion, with strain mismatch providing strong resistance to dislocation motion thereby enhancing microhardness Vickers. Furthermore, the size and morphology of the γ'' precipitates tend to be fine and disc shaped with high aspect ratios, resulting in effective dislocation motion barriers. Due to the predominantly coherent nature, γ'' forms a strong bond with the γ matrix, reducing its shear ability. Additionally, the antiphase boundaries (APBs) formed between the γ matrix and γ'' aid in local lattice strain, mechanically strengthening the material further. On the other hand, although γ' has high coherency with the matrix, the lattice mismatch between γ' and γ is relatively low and although it still contributes to mechanical strengthening via mechanisms such as Orowan strengthening, the resulting strain fields are less intense than those in γ''. Grain size hardening according to the Hall-Petch relationship can be assumed to not be the primary hardening mechanism here since the grain size of 718 is significantly larger than the 718Plus counterpart yet exhibits a

higher microhardness Vickers [35]. Furthermore, when examining both substrate materials, there appears to be more η phase present in the 718Plus substrate than there is δ phase in the 718 substrate. As these phases hold precipitate strengthening forming elements such as Nb, as well as Ti in the case of η phase, it can be theorised that a higher AF% of either of these phases in the respective substrates leads to less availability of strengthening precipitate forming elements and therefore a lower microhardness Vickers. Thus, with the 718Plus substrate having a higher amount of the η phase, there is less γ′ and γ″ formation upon ageing even with the higher temperature and longer ageing times. Likewise, less strengthening precipitates form as the ageing temperature is below the solvus of η phase and does not free up any additional forming elements for subsequent γ′ and γ″ precipitation.

The behaviour observed in the LBP-DED material is more straightforward, as both specimens were repaired using 718Plus but subjected to different ageing treatments. The HTB specimen with higher temperatures and longer durations allows enhanced diffusion of elements such as Nb, Ti and Al, acting as the driving force for nucleation and growth of γ′ and γ″ (primarily γ′). It is also well established that as ageing time and temperature increases, the size of the precipitates increase via coalescence, thereby decreasing the number of precipitates [36]. With increased precipitate size, the required stress to cut them also increases, resulting in higher microhardness Vickers. However, this applies only up to a critical precipitate size. Santos-Guemes et al. [37] found that this critical size in spherical precipitates is approximately 40 nm, yet when these features were measured from Fig. 5, the precipitates in this research are smaller (measured to be on average 31.07 nm in diameter in the HTB condition). Therefore, it is unlikely that the Orowan mechanism which causes dislocation bowing and reduction in the microhardness Vickers is a factor to consider in this material. However, Chang-Feng et al. [38] showed that when allowing for different morphologies, such as ellipsoidal in the case of γ″, this critical size is reduced to 20 nm in Alloy 718. Confirmation is difficult due to the overlapping nature of the strengthening precipitates, however, as the precipitates here are predominantly fine and near-spherical, the critical size of 40 nm is considered most vital. Thus, in this material in both heat treatment regimens, the Friedel effect causing dislocation cutting is the dominant mechanism contributing to increased microhardness Vickers due to the small precipitate size of the γ′ precipitates [37]. Yet the γ″ precipitates may decrease microhardness Vickers comparatively due to potential Orowan looping occurring at a lower critical size for these precipitates, but this is likely limited due to the small amount present in the microstructure. It can be suggested that the higher temperature and duration of the HTB specimen led to larger γ′ precipitates and an increase in microhardness Vickers but is not sufficient to 'over-age' the precipitates leading to dislocation bowing which would decrease the microhardness Vickers of the material. Notably the 718-718Plus HTA repaired specimen showed a much closer microhardness Vickers trend between the substrate and LBP-DED zone, potentially suggesting that the microhardness Vickers properties are more closely aligned across the specimen, in comparison to the 718Plus-718Plus HTB specimen.

3.3.2. Tensile

The results from the room and elevated temperature tensile tests are compiled in Fig. 15 and Table 5. At 650 °C, the strength-based properties (ultimate tensile stress (UTS) and proof stress) of both material types decreased, but with an increase in ductility, when compared to their respective behaviours at room temperature. Comparing the two repair configurations, the 718Plus-718Plus HTB specimen showed a higher UTS at both RT and 650 °C compared to the 718-718Plus HTA material. The property with the most significant difference between the two is strain at failure (SaF). At room temperature, the SaF values are comparable, however, at 650 °C the 718Plus-718Plus HTB specimen underperforms as the strain at failure of the 718-718Plus HTA specimen was almost double that of the HTB.

To investigate the fracture mechanisms of the specimens at both RT and 650 °C, the fracture surfaces were examined as presented in Fig. 16. The fracture morphologies of all specimens displayed a predominantly ductile fracture, with extensive dimpling visible as highlighted in Fig. 16e), whilst porosity was also observed throughout the surface of the fracture. In addition to this, large cracks were observed throughout the fracture surfaces, which were frequently associated with the segregated interdendritic regions of the LBP-DED material. Both the HTA and HTB post deposition heat treatments are found to be insufficient to achieve homogenisation; therefore, micro segregation and the brittle Laves phase remains in the microstructure in the interdendritic regions. Under tensile loading, these regions are likely to fracture more readily than the γ matrix, leading to regions of cracking throughout the surface of the fracture while the γ matrix deforms more typically due to tensile deformation. The large, deep cracks likely formed in regions containing a majority of Laves phase connected in a network, allowing for deeper penetrating cracks. In general, the elevated temperature specimens exhibited larger cracks and more extensive local deformation than the room temperature specimens.

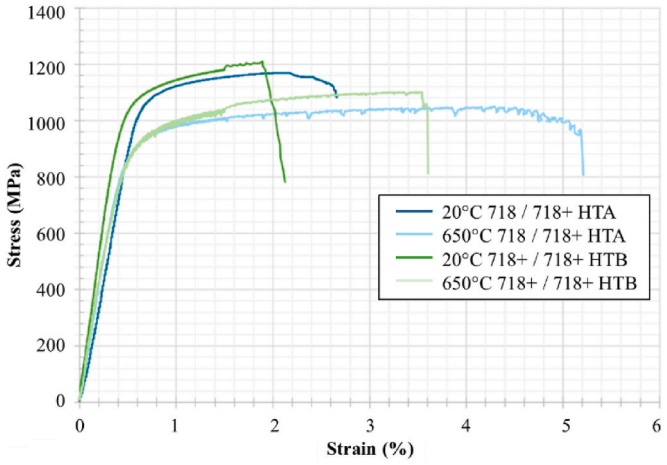

Fig. 15. Engineering stress-strain curve showing tensile behaviour of 718-718Plus HTA LBP-DED and 718Plus-718Plus HTB LBP-DED materials at RT and 650 °C.

Table 5
Mechanical properties derived from tensile tests on 718-718Plus HTA LBP-DED and 718Plus-718Plus HTB LBP-DED materials at RT and 650 °C.

Substrate/Heat Treatment	Temp. (°C)	0.2 P S (MPa)	UTS (MPa)	SaF %
718-718Plus HTA LBP-DED	20	1087	1169.36	2.66
718-718Plus HTA LBP-DED	650	924	1049.59	5.21
718Plus-718Plus HTB LBP-DED	20	1086	1208.96	2.76
718Plus-718Plus HTB LBP-DED	650	928	1101.44	3.61

EDS elemental mapping was used to further examine the fracture surface chemistry and is shown in Fig. 17. The maps show regions of Nb and Mo segregation aligned in a dendritic pattern, consistent with the Laves phase present in the interdendritic region of the microstructure. Moreover, some of the dimples present on the fracture surface exhibited residual particles, as indicated by the point scans (labelled spectrum 4 and spectrum 5) in Fig. 17, each of which displayed a high concentration of Nb and Mo. These observations are consistent with identification of these particles as Laves phase.

To further explore the fracture path of the specimens, the longitudinal fractures were examined. Macroscopic images of the fractures are shown in Fig. 18 and indicate that all specimens failed in the repaired LBP-DED zone. The high temperature testing of both 718-718Plus HTA and 718Plus-718Plus HTB specimens exhibited more extensive plastic

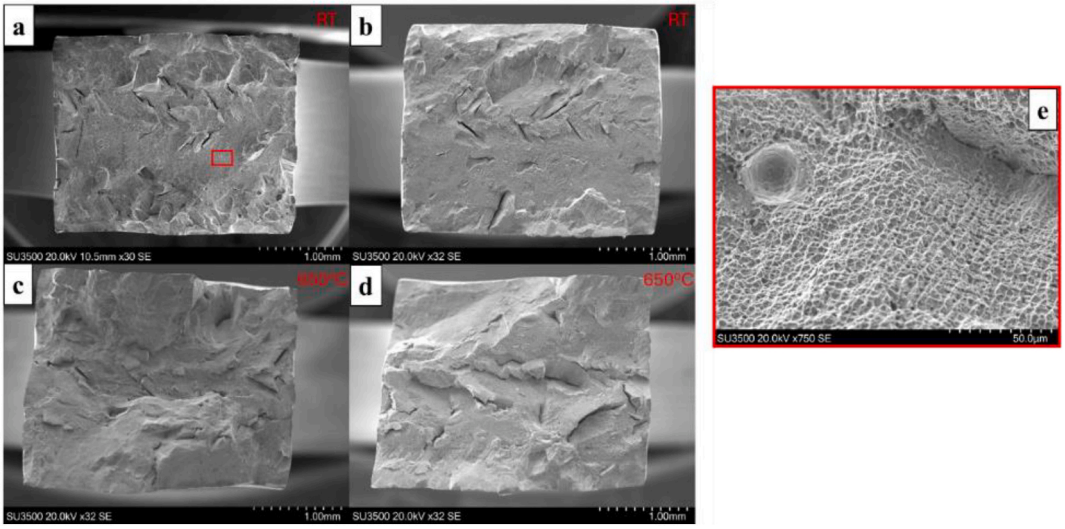

Fig. 16. Fractography of RT **a)** 718-718Plus HTA **b)** 718Plus-718Plus HTB fractured samples, and 650 °C**)** 718-718Plus HTA **d)** 718Plus-718Plus HTB samples. **e)** dimpling and porosity in RT 718-718Plus HTA sample.

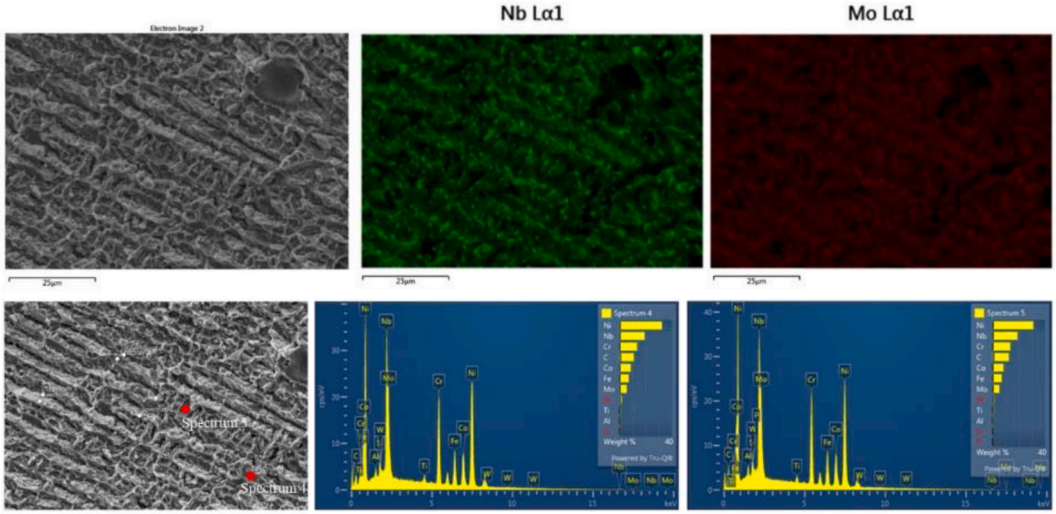

Spectrum No.	Nb (wt%)	Mo (wt%)
4	19.06	5.45
5	19.02	5.17

Fig. 17. EDS elemental maps and point scans showing Nb and Mo segregation and residual Laves phase at a pore feature in 718Plus-718Plus HTB specimen.

deformation, as indicated by increased tearing and stretching, in comparison to the RT tests, as seen in Fig. 15. The tests at elevated temperature also showed more evidence of large-scale cracks (see Fig. 18d) and h)).

Fig. 19 presents Kernel Average Misorientation (KAM) maps of the different samples. KAM is commonly used as a qualitative indicator of local lattice distortion, deformation heterogeneity, and geometrically necessary dislocation (GND) density, and can therefore provide insight into the distribution of plastic strain within the deformed material. Using local misorientation distribution the mean KAM for the 718-718Plus specimens increased from 0.59° at room temperature to 0.69° at 650 °C, for the 718Plus-718Plus specimens, whilst the mean KAM increased from 0.53° at room temperature to 0.59° at 650 °C. The maps indicate elevated KAM values in the interdendritic regions, which may be associated with microstructural heterogeneities in these areas, including the presence of brittle Laves phase and, where present, Widmanstätten η phase structures that can impede dislocation motion. In addition, the region adjacent to the fracture surface exhibits a greater fraction of higher KAM regions, shown in green in Fig. 19, consistent with increased local lattice rotation arising from strain localization during deformation. At 650 °C, enhanced dislocation mobility and increased slip activity are expected to promote more heterogeneous intragranular deformation, which can contribute to the higher KAM values observed. Although this temperature is unlikely to induce substantial recrystallisation under the present test conditions, some degree of dynamic recovery may occur, allowing dislocation rearrangement and the development of substructure, which may also influence the local misorientation. This interpretation is consistent with the thermal softening reflected by the reduced proof stress measured during the elevated-temperature tests in Table 5 [39].

Further examination of the longitudinal fracture of room temperature tested 718-718Plus, as seen in Fig. 20a), reveals the Laves phase near the point of fracture is broken and separated from the γ matrix, leading to the formation of cracks. The breaking up of the long chain-like Laves phase near the surface resulted in smaller Laves phase fragments, whereas the already small granular Laves phase appeared to maintain its

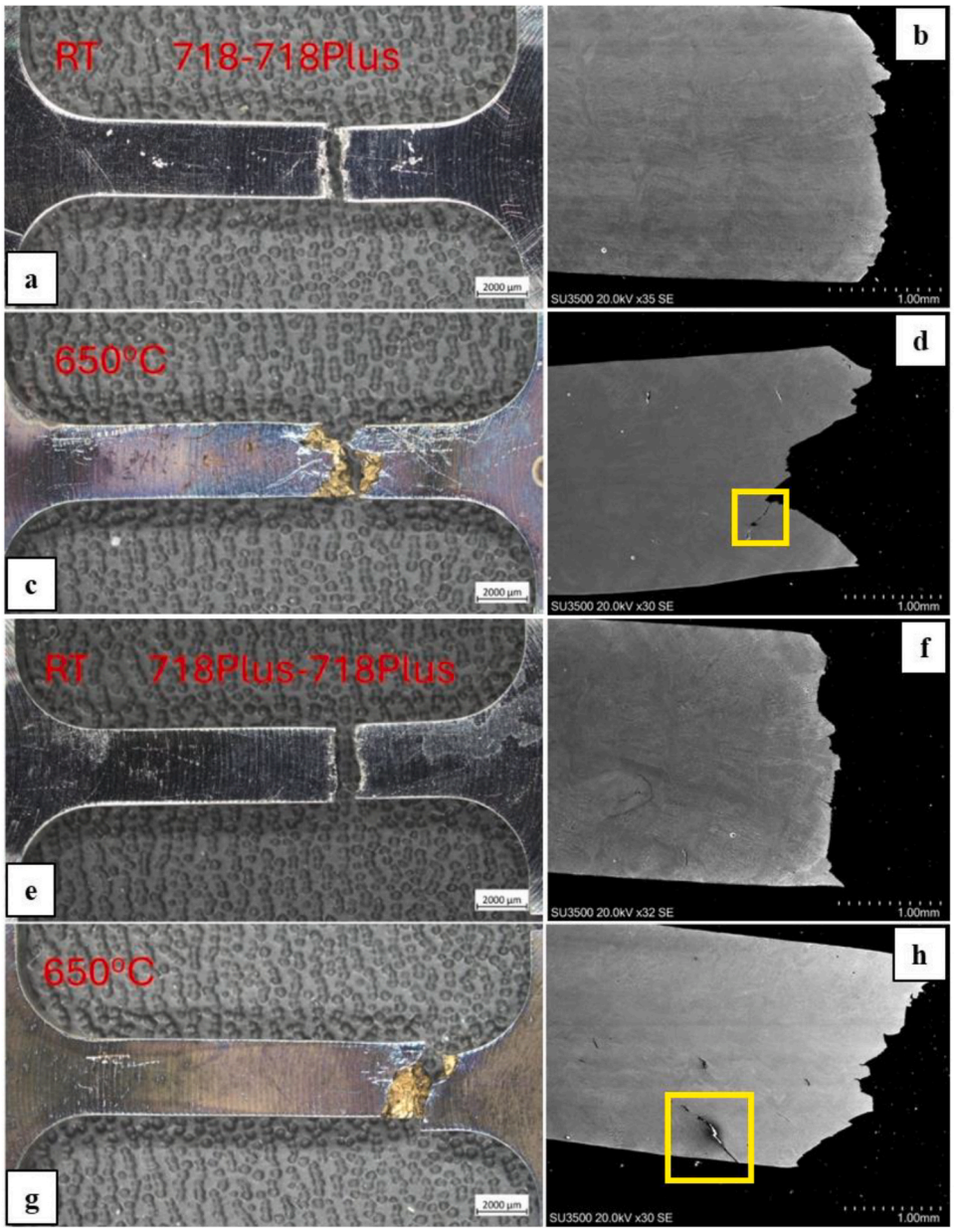

Fig. 18. Macroscopic Longitudinal view of the tensile fractures and longitudinal fracture of RT and 650 °C SEM (a) RT 718-718Plus, (b) RT 718-718Plus SEM, (c) 650 °C 718-718Plus (d) 650 °C 718-718Plus SEM, (e) RT 718Plus-718Plus, (f) RT 718Plus-718Plus SEM, (g) 650 °C 718Plus-718Plus, and (h) 650 °C 718Plus-718Plus SEM. Yellow boxes denote large cracking present in high temperature tensile tested specimens.

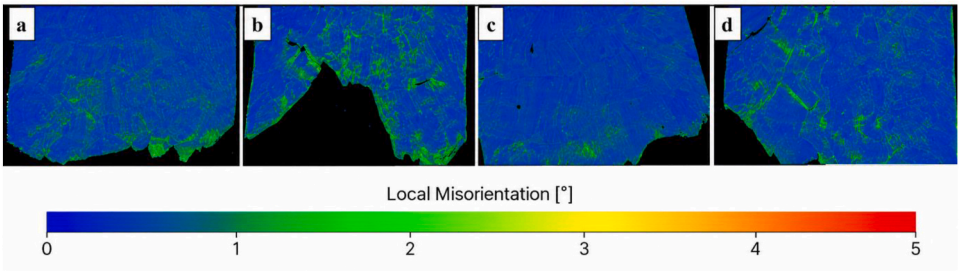

Fig. 19. KAM maps at fracture region of **a)** RT 718-718Plus, **b)** 650 °C 718-718Plus, **c)** RT 718Plus-718Plus and **d)** 650 °C 718Plus-718Plus.

morphology and simply separate from the γ matrix. Further away from the fracture site microscopic cavity-like features are present at the interface of the Laves phase due to tensile deformation as seen in Fig. 20d). With continued deformation, more of these features are likely created which will eventually coalesce and form cracks aligning with Laves phase networks, as seen in Fig. 20c). This process likely occurred

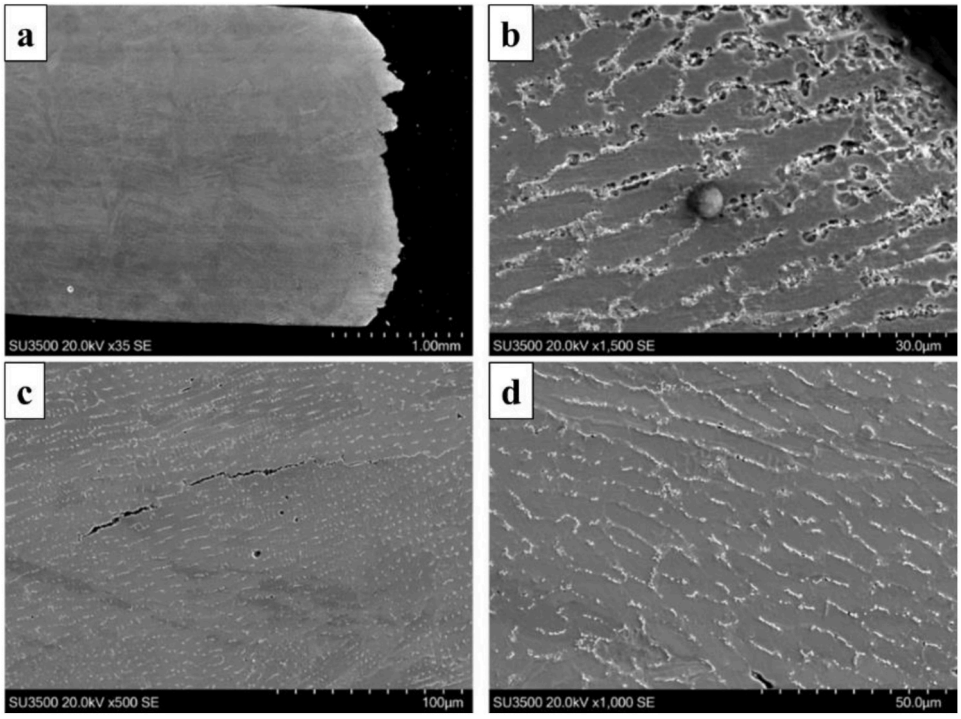

Fig. 20. Fracture surface of 718-718Plus HTA LBP-DED RT sample tested at RT **a)** overview **b)** at fracture **c)** crack along laves phase, and **d)** different morphology of Laves phase.

to a higher degree near the fracture surface which is what led to fracture occurring.

Further away from fracture, at the bond line of the substrate and LBP-DED repair zone, cracks were observed to develop along Nb-rich grain boundaries as seen in Fig. 21. Furthermore, carbides near the bond line showed evidence of cracking. Fig. 21a) shows more evidence of GB cracking visible near the bond line, indicating a clear preference for cracking at these Nb-rich grain boundaries. The substrate zone also exhibited linear features that may be consistent with twinning; however, this was not quantified crystallographically and is therefore not discussed further.

4. Mechanistic Understanding

All specimens fractured within the LBP-DED repair zone during tensile loading, with failure governed primarily by the presence of Laves phase. Microscopic cavitation was found to form at the Laves phase matrix interface, leading to cracks and ultimately failure. EDS and microstructural analysis indicate that micro segregation occurs which leads to non-uniform formation of Laves phase and strengthening precipitates preferentially in the interdendritic regions. These strengthening precipitates form more densely around the Laves phase with a more limited quantity located in the dendrite core. Thus, during tensile deformation, dislocations are likely to move more readily within the dendrite core. By contrast, the higher precipitate density adjacent to the Laves phase acts as a barrier to dislocation motion, promoting local

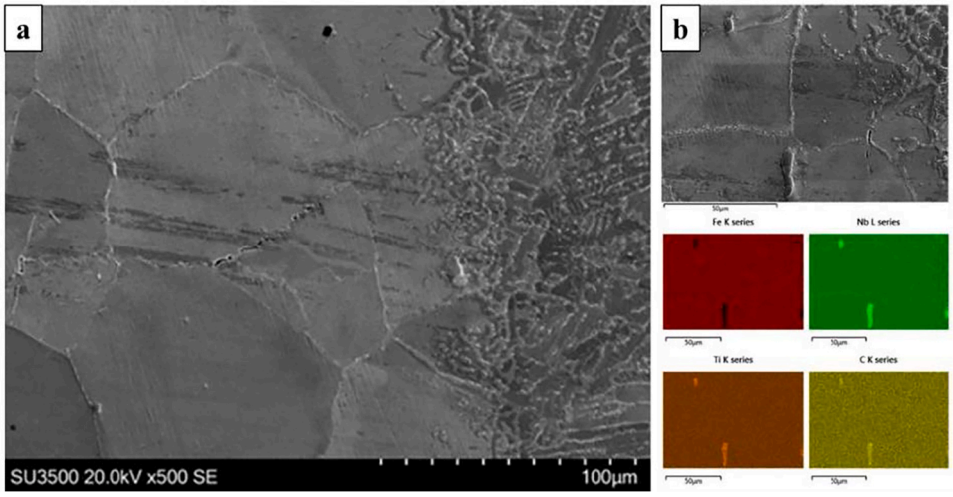

Fig. 21. A) Grain boundary cracking in the substrate near the bond line zone of the 718-718Plus HTA LBP-DED RT sample and **b)** EDS elemental maps of the bond line showing Nb-rich grain boundary cracking.

dislocation accumulation [40], as indicated by the KAM maps in Fig. 19. This would likely lead to a stress concentration at the interface between the Laves phase and γ matrix [41,42]. Since the Laves phase is inherently brittle with limited capacity for deformation [43,44] unlike the γ matrix, stress will continue to build around the Laves phase, progressing until the critical resolved shear stress is achieved and the Laves phase itself slips and fractures [45], thereby promoting cavitation, crack formation and ultimately fracture [46,47]. This behaviour is observed around the larger chain-like morphology Laves phase; however, the smaller granular Laves phase exhibited different characteristics. Due to their smaller size, the Laves phase in this case could likely deform to some degree within the γ matrix. In doing so, an element of stress is likely to be relieved around the phase, thus the critical stress required for fracture is less readily reached and breakage is less likely to occur. However, it has been observed that very close to the fracture surface, even Laves phase with a granular morphology broke, likely due to the local stress state varying with position in the fractured specimen, with higher stress likely accumulating closer to the fracture. Previous research by Sui et al. [11] and Gurland et al. [48] showed that cracking of the Laves phase was not random, and that cracking occurred perpendicular to the applied test, which aligns with the results seen in this research. Gurland et al. [48] showed that cracking occurred preferentially on planes that are normal to the maximum principal stress direction. Likewise, Sui et al. [10,11] identified that cracking in the Laves phase preferentially occurred in Laves phase that are orientated along the tensile axis, akin to the current findings here. However, in certain regions, Laves phase was found to be orientated in other directions with limited cracking occurring around the phase in these instances.

Sui et al. [11] further explored the tendency of Laves phase fracture and showed that the likelihood of fracture increased towards the centre of the long chain-like morphology. They showed that this cannot be explained by the dislocation pile up mechanism as the mechanism predicts random crack distribution with no preference as to crack location along the length of the Laves phase chain. Moreover, there is a preference for cracking in Laves phase orientated along the tensile axis, which is inconsistent with the pile up mechanism which would suggest an equal chance of cracking from the parallel to perpendicular orientation. Sui et al. [11] suggested that the fibre loading mechanism gives a more accurate prediction of Laves phase fracture. This mechanism proposes that during deformation, shear stresses exerted on the particle (in this case the Laves phase) by the deforming γ matrix are balanced by a tensile force of the non-deforming Laves phase. The fibre loading mechanism suggests that the stress within the non-deforming particle increases with distance from the particle ends; thus, stress peaks at the centre, with the maximum internal stress related to the imposed plastic strain. Therefore, when orientated along the tensile direction, particles/phases crack and fracture more readily. This mechanism aligns well with the fracture behaviour observed in the present work. It also explains why the morphology of the Laves phase influences the fracture behaviour. Sui et al. suggest that smaller granular Laves phase is less prone to cracking than the same phase in a long-chain morphology [49]. Moreover, as shown by Sui et al. [11] and Goods and Brown [50], particles that are equiaxed under deformation typically undergo interfacial decohesion, whereas, longer irregularly shaped particles fail via internal fracture, again consistent with the results obtained in the present study. Therefore, the Laves phase in the tested specimens in this research, failed either by interfacial decohesion or by internal fracture, depending on whether the morphology was granular or chain-like. It should be noted that in the present work, the orientation effect refers primarily to the morphological alignment of the Laves phase relative to the tensile loading direction, rather than to a directly measured crystallographic orientation relationship, since crystallographic indexing of the Laves phase was not performed. Nevertheless, the results indicate that chain-like Laves phase aligned close to the tensile axis behave as a brittle load-bearing inclusion, with tensile stress concentrating toward the centre of the elongated phase and promoting internal fracture. In contrast, smaller granular Laves phase produces a more localised matrix/particle strain mismatch and is therefore more likely to fail by interfacial decohesion at the γ/Laves interface.

The bond line of the specimens also consistently exhibited cracking at Nb-rich grain boundaries. As shown in Fig. 21, these regions displayed a Laves-like composition and are consistent with brittle, low-ductility boundary products. As discussed, these Nb-rich grain boundaries are considered likely to arise from the partial melting, or constitutional liquation, of NbC during the LBP-DED process, resulting in the formation of a liquid film [19]. Upon cooling, these liquated regions resolidify, producing a microstructure and composition distinct from the surrounding matrix, this is a common occurrence in Nb-rich superalloys [19,51–53]. In the LBP-DED thermal cycle, rapid heating can raise the local temperature near Nb-rich MC carbides to a point where the carbide does not fully dissolve but instead reacts locally with the surrounding γ matrix to form a Nb-enriched liquid film. As Nb segregates strongly to the remaining liquid during solidification, this film solidifies as a Laves-like constituent along grain boundaries or interdendritic regions. These resolidified constituents are brittle and chemically different from the surrounding γ matrix producing a mismatch in elastic and plastic response. During tensile loading, plastic deformation is accommodated mainly by the γ matrix, while the Nb-rich boundary constituents resist deformation. This strain incompatibility promotes dislocation pile-up and local stress concentration at the film/matrix interface, allowing cracks to nucleate along the grain boundary. Therefore, constitutional liquation does not only modify the local chemistry of the bond-line region but also creates preferential crack initiation sites under mechanical loading.

Under tensile loading, such regions are less able to accommodate deformation, thereby promoting cracking. Like the Laves phase present in the LBP-DED material, dislocations may accumulate at these interfaces during deformation, further promoting crack initiation, while their location along grain boundaries facilitates crack propagation. Pepe and Savage first proposed the mechanism of constitutional liquation [54], whereby rapid heating above the solvus temperature prevents complete dissolution of larger particles into the matrix. On subsequent heating to the eutectic temperature, the residual particle reacts with the surrounding matrix to form a liquid eutectic at the interface, and continued heating permits further particle dissolution and additional liquid formation. Constitutional liquation of this type has been widely reported in Ni-based superalloys and is particularly associated with MC carbides and Laves phase in Alloy 718 [55,56]. Nevertheless, although cracking in these regions occurred consistently, the cracks did not appear to propagate extensively or contribute to the final fracture of the specimens.

A similar phenomenon was observed for the carbides in the vicinity of the bond line. The Nb- and Ti-rich carbides are hard and brittle, and therefore deform far less readily than the surrounding matrix under tensile loading. This results in a strain incompatibility at the carbide-matrix interface, generating localised stresses that may exceed the fracture strength of the carbide or the interfacial strength, thereby leading to carbide fracture or interfacial decohesion. However, similar to the Nb-rich grain boundary cracks, carbide cracking did not appear to contribute significantly to the ultimate failure of the LBP-DED zone.

To interpret the ductility difference between the two heat-treated specimens, grain characteristics must first be considered. The grain size of both the substrate material and the LBP-DED material of the 718-718Plus HTA specimen exhibited significantly larger grains than the 718Plus-718Plus HTB specimen, as shown in Table 4. As described by the Hall-Petch equation shown in Eq. (3), smaller grains indicate more grain boundaries which would act as barriers to dislocation motion. While this would typically increase mechanical strength, grain size alone is unlikely to fully explain the ductility differences observed, moreover, the grain boundaries may act as nucleation sites for cracking, especially under tensile loading. Therefore, the coarser-grained 718-718Plus HTA sample may permit less restricted plastic deformation;

however, this effect should be considered as one contributing factor alongside differences in precipitation state and brittle constituent distribution.

$$\sigma_y = \sigma_0 + kd^{-1/2} \quad (3)$$

Where σ_y is the yield strength (MPa), σ_0 is the friction stress (MPa), k (MPa·mm^{½}) is the Hall-Petch slope constant, and d is the average grain diameter (μm).

Although the grain size in the forged substrate material for each specimen is determined by its previous processing and post-processing history, the LBP-DED material of each (inclusive of transition region) possesses a similar thermal history regarding LBP-DED processing, with only the applied heat treatment being different. Both applied heat treatments are not sufficient to induce grain growth. One possible explanation is that the grain size of LBP-DED is related to the substrate grain size. As discussed, in LBP-DED repair, the initial layers tend to grow epitaxially from the substrate, and when the substrate has large grains the newly developed deposited material inherits the orientation and some of the morphological characteristic of the substrate grains. With larger substrate grains, fewer grain boundaries are present and fewer competing growth origins are available, since the molten pools created during the LBP-DED process partially remelt the substrate and grows new grains upwards in an aligned manner. Alternatively, the epitaxial growth occurs in each grain and with a lower density of grains in the 718 forged substrate, the grains that grow from them grow to a greater extent. This is supported by previous research on deposition processes for Ni based superalloys, where it has been demonstrated that increased nucleation site density (stemming from a fine-grained substrate) leads to a refined microstructure in the deposit [18,34,57,58].

Grain boundary precipitates are a factor to consider when assessing the differing ductility of the two heat-treated samples. As discussed in section 3.1.1, there is a higher fraction of η precipitates in the repair zone of the HTB specimen, which subsequently increases Widmanstätten-like structures and decreases local ductility in the additive region of the repair. However, precipitation in the substrate must also be considered. Although δ and η are distinct phases, both precipitate preferentially at grain boundaries and can influence grain boundary mobility and mechanical response. Both δ and η phase precipitates act to pin grain boundaries, thereby limiting grain growth. This refinement in grain size would typically enhance yield strength. However, an excessive amount of either phase is likely to reduce ductility. Considering the differences in AF% of both δ and η phase shown in Table 3, the significantly higher AF% of η at grain boundaries is likely to be a contributing factor in HTB specimens, reducing ductility at both RT and high temperature when compared to the 718-718Plus HTA specimen.

At 650 °C, the γ matrix can deform more readily since dislocations have greater mobility. This is expected to occur most easily in the dendrite-core regions, where fewer strengthening precipitates and brittle phases are present. However, deformation is still not uniform across the LBP-DED microstructure. The interdendritic regions contain a greater concentration of strengthening precipitates, Laves phase, and Widmanstätten-like η phase, all of which restrict slip and deform less readily than the surrounding γ matrix. As deformation proceeds, strain is therefore concentrated in the softer γ matrix and interrupted at the brittle phase/γ matrix interfaces. This promotes local dislocation accumulation and strain gradients around the Laves and η phases. Although some dynamic recovery may occur at 650 °C, allowing partial rearrangement of dislocations in the γ matrix, it is unlikely to fully relieve the stresses built up at these interfaces. As a result, local stress concentrations develop around chain-like Laves phase and Widmanstätten η, encouraging microvoid formation, interfacial decohesion, and brittle phase cracking during tensile loading. This helps explain why fracture remains strongly associated with the interdendritic regions, even though the specimens show improved ductility at elevated temperature.

Examining the stress-strain curves in Fig. 15, a notable feature is observed, namely serrated yielding in the elevated temperature tensile tests. This behaviour is often referred to as the Portevin–Le Chatelier (PLC) effect [59–61]. This effect appears as repeated drops and rises in flow stress, corresponding to localised strain bursts. Typically, there are three classical types of serrations observed in PLC [62], as described in Table 6.

Fig. 22 shows an enhanced view of the PLC effect seen in both specimens tested at 650 °C. In both specimens, there appears to be a mixture of type A and type B serrations. Type A is characterised by smaller, more regular stress drops and occurs at higher strain rates, whereas type B is characterised by larger, less regular stress drops and typically occurs at medium strain rates.

The serrated flow is attributed to dynamic strain ageing (DSA), which occurs when diffusing solute atoms interact with dislocations during plastic deformation, effectively pinning the dislocations temporarily. Solute atoms in the material diffuse toward the mobile dislocations, since the solutes are attracted to dislocation cores due to lattice strain fields and the dislocations are temporarily pinned, necessitating a local increase in stress. Eventually, the pinned dislocation breaks free of the solute atoms, and the stored stress is released, which gives rise to serrations in the stress-strain curves. DSA in Alloy 718 typically occurs between 300 and 700 °C, with May et al. [63] reporting similar DSA occurrence in additively manufactured superalloys. The solute atoms which pin dislocations must not be locked up by precipitates and instead must remain available in the solid solution. Therefore, increased γ′ and γ″ precipitation reduces the number of solute atoms such as Nb, C, N and Ti available in the matrix, thereby reducing susceptibility to DSA. Nevertheless, some solute atoms will remain in the solid solution allowing DSA to occur, therefore, the higher precipitation state in the HTB specimen may reduce the DSA response and contribute to the reduced serrations observed, although its higher UTS is more appropriately attributed to its overall strengthening state. This can be seen in Fig. 22, in which the HTA specimen shows a greater degree of serrated flow due to a higher availability of diffusing solute atoms. Nalawade et al. [64] showed that at high temperatures, DSA occurs in Alloy 718 due to the diffusion of Nb solute atoms rather than by any interstitial atoms, which explains why less DSA occurs in the HTB specimen due to the Nb being locked into strengthening precipitates [65].

5. Conclusions

The present research has explored the effects of different heat treatments on the microstructure and mechanical properties of 718 and 718Plus forged substrate materials repaired by directed energy deposition by laser with 718Plus. The main conclusions are as follows.

1. Both repaired configurations contained distinct substrate, heat-affected zone, bond-line and LBP-DED repair zones. The forged substrates exhibited equiaxed grain structures, with δ phase observed in Alloy 718 and η phase observed in Alloy 718Plus. The HAZ showed local grain coarsening and a reduction in grain-boundary secondary phases, indicating the influence of the LBP-DED thermal cycle.
2. The LBP-DED repair zone retained a columnar dendritic structure with interdendritic Laves phase in both chain-like and granular morphologies. The ageing heat treatments promoted nanoscale

Table 6
Types of portevin-le chatelier effect.

Type	Description	Common in
Type A	Regular, sharp serrations -dislocations move one by one.	Higher strain rates
Type B	Irregular serrations, appearing as bursts.	Medium strain rates
Type C	Large stress drops, static strain localization.	Lower strain rates

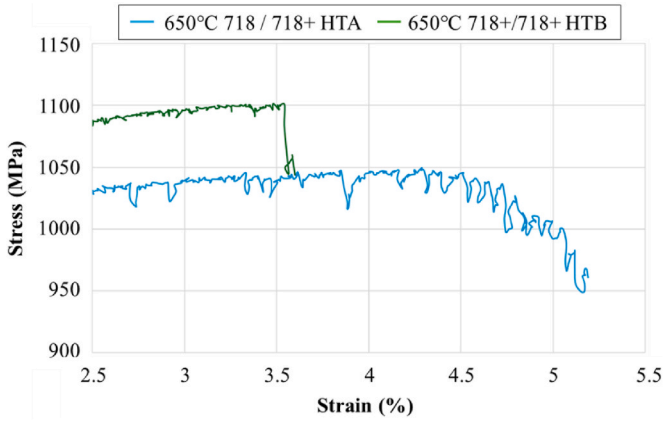

Fig. 22. Magnified view of elevated temperature tensile tests on 718-718Plus HTA LBP-DED, and 718Plus-718Plus HTB LBP-DED specimens, illustrating the presence of PLC.

strengthening precipitates and local needle-like η phase formation near Laves phase regions. The standard Alloy 718Plus heat treatment produced a more developed precipitation state than the Alloy 718 heat treatment due to its higher temperature and longer duration. However, neither heat treatment produced a substantial change in grain size or DAS under the conditions examined.

3. The initial forged substrate microstructure strongly influenced epitaxial growth in the LBP-DED repair material. The coarser forged Alloy 718 substrate promoted larger LBP-DED grains, whereas the finer forged Alloy 718Plus substrate resulted in comparatively finer repair zone grains. This indicates that the final LBP-DED grain structure was governed more strongly by the substrate grain structure and the inherited as-deposited condition than by the applied ageing heat treatment.
4. The repaired specimens exhibited broadly similar tensile behaviour at room temperature. At 650 °C, the 718-718Plus HTA condition exhibited higher ductility, while the 718Plus-718Plus HTB condition showed higher ultimate tensile strength but reduced strain to failure. This suggests that differences in grain structure, precipitation state and local microstructural heterogeneity influenced the elevated-temperature mechanical response.
5. Failure occurred within the LBP-DED repair zone in all specimens and was strongly associated with interdendritic Laves phase. Chain-like Laves phase promoted cracking and crack linkage, whereas granular Laves phase more commonly showed interfacial decohesion from the γ matrix. Serrated yielding was observed at 650 °C in both repair conditions, indicating dynamic strain ageing; this effect was more pronounced in the HTA condition, likely due to greater solute availability in the matrix.
6. Overall, the results show that the two ageing heat treatments produced only limited differences in the LBP-DED Alloy 718Plus repair material. The initial forged substrate microstructure and the as-deposited LBP-DED solidification structure had a stronger influence on the final repair zone microstructure and elevated-temperature mechanical behaviour. Therefore, substrate condition should be carefully considered when designing Alloy 718Plus LBP-DED repair strategies for forged Alloy 718 and Alloy 718Plus components.

Declaration of competing interest

The authors declare that they have no known competing financial interests or personal relationships that could have appeared to influence the work reported in this paper.

Acknowledgements

The current research was funded under the EPSRC Industrial Case Award EP/W524694/1. The provisions of research bursary, materials, and supporting information from Rolls-Royce plc. Is gratefully acknowledged. Mechanical tests were performed at SMaRT. Utilisation of the FEG-SEM was provided by Swansea University's Advanced Imaging of Materials (AIM) Facility, which was funded by the EPSRC (EP/M028267/1), The European Regional Development Fund through the Welsh Government (80708) and the Ser Solar project via the Welsh Government.

Data availability

The raw/processed data required to reproduce these findings cannot be shared at this time as the data also forms part of an ongoing study.

References

[1] Hosseini E, Popovich VA. A review of mechanical properties of additively manufactured Inconel 718. Addit Manuf 2019;30:100877. https://doi.org/10.1016/j.addma.2019.100877.
[2] Nickel alloy, corrosion and heat resistant, bars, forgings, and rings 52.5Ni 19Cr 3.0Mo 5.1Cb 0.90Ti 0.50Al 18Fe, consumable electrode or vacuum induction melted 1775°F (968°C) solution heat treated. Warrendale, PA, United States: Precipitation Hardenable. 400 Commonwealth Drive; 1965. https://doi.org/10.4271/AMS5662.
[3] Ding Q, Lao Z, Wei H, Li J, Bei H, Zhang Z. Site occupancy of alloying elements in γ′ phase of nickel-base single crystal superalloys. Intermetallics 2020;121:106772. https://doi.org/10.1016/j.intermet.2020.106772.
[4] Li W, Terret D, McDevitt E, Ndoye S, Gardner S. Development of ATI 718Plus® for high temperature high strength fastener applications. In: 8th international symposium on superalloy 718 and derivatives. Wiley; 2014. p. 503–20. https://doi.org/10.1002/9781119016854.ch40.
[5] Cao W Di, Kennedy R. Role of chemistry in 718-type alloys - allvac® 718plus™ alloy development. In: Proceedings of the international symposium on superalloys; 2004. https://doi.org/10.7449/2004/superalloys_2004_91_99.
[6] 625, 706 and Various Derivatives (2005), TMS Kennedy RL. Allvac 718Plus, superalloy for the next forty years. Superalloys 2005;718. https://doi.org/10.7449/2005/Superalloys_2005_1_14. 1–14.
[7] Gebisa AW, Lemu HG. Additive manufacturing for the manufacture of gas turbine engine components: literature review and future perspectives. In: Proceedings of the ASME turbo expo, vol. 6; 2018. https://doi.org/10.1115/GT2018-76686.
[8] Svetlizky D, Das M, Zheng B, Vyatskikh AL, Bose S, Bandyopadhyay A, et al. Directed energy deposition (DED) additive manufacturing: physical characteristics, defects, challenges and applications. Mater Today 2021;49:271–95. https://doi.org/10.1016/j.mattod.2021.03.020.
[9] Sui S, Li Z, Zhong C, Zhang Q, Gasser A, Chen J, et al. Laves phase tuning for enhancing high temperature mechanical property improvement in laser directed energy deposited Inconel 718. Compos B Eng 2021;215. https://doi.org/10.1016/j.compositesb.2021.108819.
[10] Sui S, Chen J, Ming X, Zhang S, Lin X, Huang W. The failure mechanism of 50% laser additive manufactured Inconel 718 and the deformation behavior of Laves phases during a tensile process. Int J Adv Manuf Technol 2017;91:2733–40. https://doi.org/10.1007/s00170-016-9901-9.
[11] Sui S, Tan H, Chen J, Zhong C, Li Z, Fan W, et al. The influence of Laves phases on the room temperature tensile properties of Inconel 718 fabricated by powder feeding laser additive manufacturing. Acta Mater 2019;164:413–27. https://doi.org/10.1016/j.actamat.2018.10.032.
[12] Sui S, Li H, Li Z, Zhao X, Ma L, Chen J. Introduction of a new method for regulating laves phases in inconel 718 superalloy during a laser-repairing process. Engineering 2022;16:239–46. https://doi.org/10.1016/j.eng.2021.08.030.
[13] Sui S, Chen J, Fan E, Yang H, Lin X, Huang W. The influence of Laves phases on the high-cycle fatigue behavior of laser additive manufactured Inconel 718. Mater Sci Eng 2017;695:6–13. https://doi.org/10.1016/j.msea.2017.03.098.
[14] Sui S, Chen J, Li Z, Li H, Zhao X, Tan H. Investigation of dissolution behavior of laves phase in inconel 718 fabricated by laser directed energy deposition. Addit Manuf 2020;32. https://doi.org/10.1016/j.addma.2020.101055.
[15] ATI 718Plus ® alloy 1 ATI 718Plus ® alloy 1 precipitation hardened nickel-base superalloy. 2013.
[16] London Aerospace series-Metallic materials-Test methods-Part 1: tensile testing at ambient temperature. 2005.
[17] Manvatkar V, De A, DebRoy T. Spatial variation of melt pool geometry, peak temperature and solidification parameters during laser assisted additive manufacturing process. Mater Sci Technol 2015;31:924–30. https://doi.org/10.1179/1743284714Y.0000000701.
[18] DebRoy T, Wei HL, Zuback JS, Mukherjee T, Elmer JW, Milewski JO, et al. Additive manufacturing of metallic components – process, structure and properties. Prog Mater Sci 2018;92:112–224. https://doi.org/10.1016/j.pmatsci.2017.10.001.

[19] Vishwakarma KR, Richards NL, Chaturvedi MC. Microstructural analysis of fusion and heat affected zones in electron beam welded ALLVAC® 718PLUS™ superalloy. Mater Sci Eng 2008;480:517–28. https://doi.org/10.1016/j.msea.2007.08.002.

[20] Chen Y, Zhang K, Huang J, Hosseini SRE, Li Z. Characterization of heat affected zone liquation cracking in laser additive manufacturing of Inconel 718. Mater Des 2016;90:586–94. https://doi.org/10.1016/j.matdes.2015.10.155.

[21] Sarkar R. Repair of nickel-base superalloy components using direct energy deposition. n.d.

[22] Liu F, Lyu F, Liu F, Lin X, Huang C. Laves phase control of inconel 718 superalloy fabricated by laser direct energy deposition via δ ageing and solution treatment. J Mater Res Technol 2020;9:9753–65. https://doi.org/10.1016/j.jmrt.2020.06.061.

[23] Huang CA, Wang TH, Lee CH, Han WC. A study of the heat-affected zone (HAZ) of an Inconel 718 sheet welded with electron-beam welding (EBW). Mater Sci Eng 2005;398:275–81. https://doi.org/10.1016/j.msea.2005.03.029.

[24] Radhakrishna C, Prasad Rao K. The formation and control of Laves phase in superalloy 718 welds. J Mater Sci 1997;32:1977–84. https://doi.org/10.1023/A:1018541915113.

[25] Zhou D, Ye X, Teng J, Li C, Li Y. Effect of Nb on microstructure and mechanical property of novel powder metallurgy superalloys during long-term thermal exposure. Materials 2021;14:656. https://doi.org/10.3390/ma14030656.

[26] Asala G, Khan AK, Andersson J, Ojo OA. Microstructural analyses of ATI 718Plus® produced by wire-ARC additive manufacturing process. Metall Mater Trans 2017;48:4211–28. https://doi.org/10.1007/s11661-017-4162-2.

[27] Dziuba O, Cempura G, Wusatowska-Sarnek A, Kruk A. Influence of isothermal holding on the microstructure and mechanical properties of electron beam welded dissimilar inconel 718/ATI 718Plus® joint. J Mater Eng Perform 2020;29:1515–21. https://doi.org/10.1007/s11665-020-04583-6.

[28] Li L, Ren Y, Chang S, Li M, Lin S, Wang M. Evaluation of the ATI 718Plus repaired by laser metal deposition under heat treatment regimes: microstructures, mechanical properties, and their heterogeneity. Mater Sci Eng 2023;885:145540. https://doi.org/10.1016/j.msea.2023.145540.

[29] Gasson PC. The superalloys: fundamentals and applications R. C. Reed cambridge university press, the Edinburgh building, shaftesbury road, cambridge, CB2 2RU, UK, 2006. 372pp. Illustrated. £80. ISBN 0-521-85904-2. Aeronaut J 2008;112:291. https://doi.org/10.1017/S0001924000087509. 291.

[30] Krakow R, Hardy MC, Rae CMF, Midgley PA. High resolution orientation mapping of secondary phases in ATI 718Plus ® alloy. MATEC Web of Conferences 2014;14:11002. https://doi.org/10.1051/matecconf/20141411002.

[31] Messe OM, Bjs PEJ, Mpa RCMF. On the precipitation of delta phase in ALLVAC® 718Plus. Philos Mag 2013;94:1132–52.

[32] Casanova A, Hardy M, Rae CMF. Morphology and kinetics of grain boundary precipitation in alloy ATI 718Plus®. In: 8th international symposium on superalloy 718 and derivatives. Wiley; 2014. p. 573–86. https://doi.org/10.1002/9781119016854.ch45.

[33] Zhai Y, Lados DA, Brown EJ, Vigilante GN. Understanding the microstructure and mechanical properties of Ti-6Al-4V and inconel 718 alloys manufactured by laser engineered net shaping. Addit Manuf 2019;27:334–44. https://doi.org/10.1016/j.addma.2019.02.017.

[34] Kurz W, Fisher DJ, Rappaz M. Fundamentals of solidification. fifth ed., 103. Trans Tech Publications Ltd; 2023. https://doi.org/10.4028/b-v7b35q.

[35] Lee GH, Kim B, Jeon JB, Park M, Noh S, Kim BJ. Precipitate phase behavior and mechanical properties of Inconel 718 according to ageing heat treatment time. Mater Sci Eng 2025;924:147776. https://doi.org/10.1016/j.msea.2024.147776.

[36] Moore IJ, Burke MG, Nuhfer NT, Palmiere EJ. Evaluation of classical precipitation descriptions for $$\gamma ^{\prime \prime } \,(\hbox {Ni}_{3}\hbox {Nb}{-}\hbox {D0}_{22})$$ γ″ (Ni 3 Nb - D0 22) in Ni-base superalloys. J Mater Sci 2017;52:8665–80. https://doi.org/10.1007/s10853-017-1091-9.

[37] Santos-Güemes R, Capolungo L, Segurado J, Llorca J. Dislocation dynamics prediction of the strength of Al-Cu alloys containing shearable θ'' precipitates. J Mech Phys Solid 2021;151:104375. https://doi.org/10.1016/j.jmps.2021.104375.

[38] Wan C-F, Sun L-G, Qin H-L, Bi Z-N, Li D-F. A molecular dynamics study on the dislocation-precipitate interaction in a nickel based superalloy during the tensile deformation. Materials 2023;16:6140. https://doi.org/10.3390/ma16186140.

[39] Tang C, Shi D, Zhang J. Temperature-induced variations in slip behavior of single crystal aluminum: microstructural analysis. Materials 2024;17:2084. https://doi.org/10.3390/ma17092084.

[40] Guo JM, Zhou BC, Qiu S, Kong HJ, Niu MC, Luan JH, et al. Achieving ultrahigh strength and ductility in high-entropy alloys via dual precipitation. J Mater Sci Technol 2023;166:67–77. https://doi.org/10.1016/j.jmst.2023.05.021.

[41] Wang K, Liu Y, Sun Z, Lin J, Lv Y, Xu B. Microstructural evolution and mechanical properties of Inconel 718 superalloy thin wall fabricated by pulsed plasma arc additive manufacturing. J Alloys Compd 2020;819:152936. https://doi.org/10.1016/j.jallcom.2019.152936.

[42] Xu L, Chai Z, Chen H, Zhang X, Xie J, Chen X. Tailoring Laves phase and mechanical properties of directed energy deposited Inconel 718 thin-wall via a gradient laser power method. Mater Sci Eng 2021;824:141822. https://doi.org/10.1016/j.msea.2021.141822.

[43] Bewlay BP, Sutliff JA, Jackson MR, Lipsitt HA. Microstructural and crystallographic relationships in directionally solidified Nb□Cr2Nb and Cr□Cr2Nb eutectics. Acta Metall Mater 1994;42:2869–78. https://doi.org/10.1016/0956-7151(94)90228-3.

[44] Zhang Z, Liu J, Guo J, Ma J, Wang X, Zhou Y, et al. Electropulsing-enhanced dissolution of Laves phase and tensile properties in laser additively manufactured 718Plus alloy. Mater Sci Eng 2025;937:148475. https://doi.org/10.1016/j.msea.2025.148475.

[45] Xu L, Chai Z, Chen H, Zhang X, Xie J, Chen X. Tailoring Laves phase and mechanical properties of directed energy deposited Inconel 718 thin-wall via a gradient laser power method. Mater Sci Eng 2021;824:141822. https://doi.org/10.1016/j.msea.2021.141822.

[46] Zhang Y-N, Cao X, Wanjara P, Medraj M. Tensile properties of laser additive manufactured Inconel 718 using filler wire. J Mater Res 2014;29:2006–20. https://doi.org/10.1557/jmr.2014.199.

[47] Sui S, Chen J, Zhang R, Ming X, Liu F, Lin X. The tensile deformation behavior of laser repaired Inconel 718 with a non-uniform microstructure. Mater Sci Eng 2017;688:480–7. https://doi.org/10.1016/j.msea.2017.01.110.

[48] Gurland J. Observations on the fracture of cementite particles in a spheroidized 1.05% c steel deformed at room temperature. Acta Metall 1972;20:735–41. https://doi.org/10.1016/0001-6160(72)90102-2.

[49] Lindley TC, Oates G, Richards CE. A critical of carbide cracking mechanisms in ferride/carbide aggregates. Acta Metall 1970;18:1127–36. https://doi.org/10.1016/0001-6160(70)90103-3.

[50] Goods SH, Brown LM. Overview No. 1. Acta Metall 1979;27:1–15. https://doi.org/10.1016/0001-6160(79)90051-8.

[51] Ariaseta A, Andersson J, Ojo O. Heat-affected zone cracking in new 718-type superalloy VDM alloy 780: effect of solution heat treatments and comparison with alloy 718. Mater Des 2025;258:114733. https://doi.org/10.1016/j.matdes.2025.114733.

[52] Ariaseta A, Andersson J, Ojo O. Weldability of new Ni-based superalloy G27: effect of pre-weld solution annealing on the hot cracking susceptibility. Sci Technol Weld Joining 2024;29:368–78. https://doi.org/10.1177/13621718241285301.

[53] Andersson J, Sjöberg GP, Viskari L, Chaturvedi MC. Effect of solution heat treatments on superalloys Part 1 – alloy 718. Mater Sci Technol 2012;28:609–19. https://doi.org/10.1179/1743284711Y.0000000101.

[54] Pepe JJ, Savage WF. Effects of constitutional liquation in 18-Ni marageing steel weldments. Weld J 1967;46. 411s–22s.

[55] Thompson EG. Hot cracking studies of alloy 718 weld heat-affected zones. Weld J. 1969.

[56] Baeslack WA, Nelson DE. Morphology of weld heat-affected zone liquation in cast alloy 718. Metallography 1986;19:371–9. https://doi.org/10.1016/0026-0800(86)90024-8.

[57] Dinda GP, Dasgupta AK, Mazumder J. Texture control during laser deposition of nickel-based superalloy. Scr Mater 2012;67:503–6. https://doi.org/10.1016/j.scriptamat.2012.06.014.

[58] Jeong SG, Ahn SY, Kim ES, Karthik GM, Baik Y, Seong D, et al. Effect of substrate yield strength and grain size on the residual stress of direct energy deposition additive manufacturing measured by neutron diffraction. Mater Sci Eng 2022;851:143632. https://doi.org/10.1016/j.msea.2022.143632.

[59] Jiang H, Zhang Q, Chen X, Chen Z, Jiang Z, Wu X, et al. Three types of portevin–le chatelier effects: experiment and modelling. Acta Mater 2007;55:2219–28. https://doi.org/10.1016/j.actamat.2006.10.029.

[60] CottrellA.H. L.X.X.X.V.IA note on the Portevin-Le Chatelier effect London, Edinburgh Dublin Phil Mag. J Sci 1953;44:829–32. https://doi.org/10.1080/14786440808520347.

[61] Yilmaz A. The Portevin–Le Chatelier effect: a review of experimental findings. Sci Technol Adv Mater 2011;12:063001. https://doi.org/10.1088/1468-6996/12/6/063001.

[62] Rowlands BS, Rae C, Galindo-Nava E. The Portevin-Le Chatelier effect in nickel-base superalloys: origins, consequences and comparison to strain ageing in other alloy systems. Prog Mater Sci 2023;132:101038. https://doi.org/10.1016/j.pmatsci.2022.101038.

[63] May PE, White M, Bordin A, Ednie L, Huff R, Vunnam S, et al. Influence of heat treatment on the high temperature properties of inconel 718 fabricated via laser beam powder bed fusion. J Mater Res Technol 2025;36:9881–97. https://doi.org/10.1016/j.jmrt.2025.05.140.

[64] Nalawade SA, Sundararaman M, Kishore R, Shah JG. The influence of ageing on the serrated yielding phenomena in a nickel-base superalloy. Scr Mater 2008;59:991–4. https://doi.org/10.1016/j.scriptamat.2008.07.004.

[65] Saravanan K, Chakravadhanula VSK, Manwatkar SK, Narayana Murty SVS, Ramesh Narayanan P. Dynamic strain ageing and embrittlement behavior of IN718 during high-temperature deformation. Metall Mater Trans 2020;51:5691–703. https://doi.org/10.1007/s11661-020-05970-3.